POLITECNICO DI TORINO
Repository ISTITUZIONALE

W-doped indium oxide synthetized via hydrothermal route for low temperature ozone sensing

Original
W-doped indium oxide synthetized via hydrothermal route for low temperature ozone sensing / Ziegler, D., Palmero, P., Tulliani, J.M.C.. - In: SOLID STATE IONICS. - ISSN 0167-2738. - ELETTRONICO. - 347:115271(2020). [10.1016/j.ssi.2020.115271]

Availability:
This version is available at: 11583/2839732 since: 2020-07-13T22:55:54Z

Publisher:
Elsevier

Published
DOI:10.1016/j.ssi.2020.115271

Terms of use:

This article is made available under terms and conditions as specified in the corresponding bibliographic description in the repository

Publisher copyright
Elsevier postprint/Author's Accepted Manuscript

© 2020. This manuscript version is made available under the CC-BY-NC-ND 4.0 license http://creativecommons.org/licenses/by-nc-nd/4.0/.The final authenticated version is available online at: http://dx.doi.org/10.1016/j.ssi.2020.115271

(Article begins on next page)

25 November 2026

Applied Surface Science Advances 29 (2025) 100837

Contents lists available at ScienceDirect

Applied Surface Science Advances

journal homepage: www.sciencedirect.com/journal/applied-surface-science-advances

Full Length Article

Titanium surface functionalization via fibrinogen-coated nano-topography: Physicochemical surface characterization and pre-osteoblastic cell response

Antônio Secco Martorano [a,*], Camilla Reggio [b], Luciana Oliveira de Almeida [c], Cristina Scolaro [d], Larissa Moreira Spinola de Castro-Raucci [e], Silvia Spriano [b], Paulo Tambasco de Oliveira [a]

[a] School of Dentistry of Ribeirão Preto, University of São Paulo, São Paulo, Brazil
[b] Department of Applied Science and Technology, Politecnico di Torino, Torino, Italy
[c] School of Pharmaceutical Sciences of Ribeirão Preto, University of São Paulo, São Paulo, Brazil
[d] Department of Engineering, University of Messina, Messina, Italy
[e] Faculty of Dentistry, University of Ribeirão Preto, São Paulo, Brazil

ARTICLE INFO

Keywords:
Titanium
Surface functionalization
Nano-topography
Fibrinogen
Cell culture
Osteoblast

ABSTRACT

The aim of this study was to evaluate fibrinogen (FG) coating on a nanostructured titanium surface (Ti) regarding its physicochemical properties and the response of pre-osteoblastic cells *in vitro*. Commercially pure Ti discs were ground and chemically treated with a 1:1 mixture of 30% hydrogen peroxide and concentrated sulfuric acid (Nano-Ti). FG coating was performed by simple adsorption at its plasma concentration (FG/Nano-Ti). Pre-osteoblastic MC3T3-E1 cells were plated on Nano-Ti and FG/Nano-Ti and cultured for up to 18 days. FG/Nano-Ti resulted in the availability of 0.7 mg/cm^2 of protein on FG/Nano-Ti (BCA). Nano-Ti and FG/Nano-Ti exhibited microscale grooves and a typical nano-topography, with a network of nanopores, which was partially masked for FG/Nano-Ti by the presence of granulated material of homogeneous distribution. The adsorbed protein layer was continuous and probably a few nanometers thick, not affecting the micro-grooves of Nano-Ti. The roughness parameters exhibited higher values for FG/Nano-Ti. Zeta potential titration curves showed an isoelectric point at pH 3.5 for Nano-Ti evidencing hydroxyl functional groups with a weak acidic reactivity and 5.5 for FG/Nano-Ti, which is the same as FG, in agreement with a continuous adsorbed layer. The presence of FG reduced the wettability of the nano-topography in contact with a drop of water or fetal bovine serum, but enhanced it when a blood drop was used. The biological results showed a higher expression of classical osteoblast markers – especially RUNX2 – on FG/Nano-Ti, which corresponded to higher values of alkaline phosphatase activity and mineralization of the cultures. When FG/Nano-Ti was exposed to exogenous thrombin, a homogeneous fibrin fibril was assembled. In conclusion, the strategy of coating FG/Nano-Ti with FG potentiates the capacity of Nano-Ti to promote osteogenic differentiation.

1. Introduction

Titanium (Ti) and its alloys are the gold standard alloplastic materials used to produce metallic implants in the field of bone implantology [1]. The ability to achieve osseointegration is due to the types of macrogeometric design of the implants, the biomechanical cues they provide, the physicochemical properties of their surfaces, and the impact these factors exert on the host tissue response [2]. Regarding the physicochemical properties, surface topography, chemistry, and energy play critical roles in determining biocompatibility and the success of osseointegration, as they directly influence endogenous protein adsorption and cell behavior [3].

Despite the major advances achieved with the development of microtopographic surfaces [4], improved biocompatibility has been observed with the creation of nano-topographies. Overall, nanostructured surfaces engineered to mimic the characteristics of natural bone have demonstrated promising results in *in vitro* studies, animal models, and clinical trials, underscoring their relevance in bone

* Corresponding author at: Department of Basic and Oral Biology, School of Dentistry of Ribeirão Preto, University of São Paulo, *Av.* do Café, s/n – Campus USP Monte Alegre, 14040-904, Ribeirão Preto, SP, Brazil.
E-mail address: antoniomartora@usp.br (A.S. Martorano).

https://doi.org/10.1016/j.apsadv.2025.100837
Received 9 June 2025; Received in revised form 17 August 2025; Accepted 26 August 2025
Available online 30 August 2025
2666-5239/© 2025 The Author(s). Published by Elsevier B.V. This is an open access article under the CC BY-NC-ND license (http://creativecommons.org/licenses/by-nc-nd/4.0/).

formation and regeneration [5–8]. *In vitro*, nanoscale surface topographies and other nanometric modifications are widely recognized for inducing significant changes in osteoblastic cell behavior, which include impacts on cell adhesion, spreading and focal adhesion formation, polarization, migration, proliferation, and differentiation – factors that potentially affect the osseointegration process [7,9–17]. Furthermore, the interaction of osteoblastic and osteoclastic cells with Ti nano-topographies has been shown to inhibit the activity and differentiation of osteoclast precursors, thereby modulating osteoblast–osteoclast crosstalk involved in bone remodeling [17].

Among the various approaches for the nanotexturing of Ti surfaces, the subtractive method of chemical treatment using equal volumes of 30 % H_2O_2 and concentrated H_2SO_4 is characterized by its simplicity and low cost, and produces a characteristic surface nanoporous network [18]. This nano-topography (Nano-Ti) has been shown to promote the early expression/secretion of the multifunctional non-collagenous proteins bone sialoprotein (BSP) and osteopontin (OPN) [9,19], and to enhance the osteogenic differentiation by (i) an increase in the focal adhesions and abundance of filopodia [20], and (ii) BMP-2 [21], (iii) integrin-mediated [13] and (iv) Wnt/β-catenin [12] signaling pathways. Taken together, these events support a higher proportion of bone-to-implant contact and a positive effect on the outcome of implants [22].

In addition to promoting molecular, cellular, and tissue effects by the nanoscale cueing per se, Ti nano-topographies can benefit from coating with bioactive organic molecules [23]. This approach combines physical and/or chemical surface modifications with the incorporation of organic molecules such as proteins, peptides, and growth factors, aiming to create biomimetic environments that regulate cellular functions and enhance interactions with the physiological milieu, thereby directing biological processes and improving the efficiency of tissue repair [24,25].

Blood clot formation is the first biological event during tissue repair at the interface with Ti implants [26,27]. Its 3D fibrin network structure supports the migration of connective tissue cells and extravasated blood cells toward the implant surface [28,29]. Given the importance of these initial events for the integration of an implant into bone, attempts have been made to promote the occurrence of a more uniform distribution of blood clot throughout the Ti surface. The strategies that have been developed to improve clot homogeneity include changes in surface roughness/topography at the micro and nano-scale and in surface chemistry/functional groups, in addition to applying coatings using organic molecules [26,30–35]. For instance, on hyperhydrophilic sand-blasted and acid-etched (SBA) Ti surfaces produced by alkali treatment, blood clots assemble in an organized and layered architecture, with a dense fibrin fiber network providing a continuous coverage of the entire surface [30]. A sandblasted and double-acid etched (SLA) surface, with a characteristic microtopography and surface chemistry, also supports the formation of a more homogeneous blood clot compared to polished Ti [31]. Titanium oxide thin films with rutile structures, created by physical vapor deposition, exhibit a higher dielectric constant, which induces the activation of factor XII in blood clotting and the formation of fibrin network [32]. An anodized Ti surface with increased nano-roughness promotes more extension of fibrin clot formation compared to an acid-etched control Ti, yet both surfaces support a non-uniform fibrin clot distribution [33]. The Nano-Ti also supports the occurrence of an inhomogeneous distribution of the 3D blood clot structure over its surface in an *in vivo* model [27] despite exhibiting nano-topography and high hydrophilicity, which are factors that are known to induce pronounced blood coagulation [36,37]. Thus, to avoid any potential negative impact on tissue formation at the interfacial region that the inhomogeneity of blood clot could promote [38], it might be relevant to coat Nano-Ti with an exogenous molecule that could contribute to the formation of a more homogeneous 3D clot. Given that fibrinogen (FG), a major plasma protein, is the key soluble precursor to fibrin fibrils – in a process depending on thrombin activity – and that its adsorption on biomaterial surfaces triggers the intrinsic pathway of blood coagulation [39], it could be a good candidate molecule for that purpose.

Fibrinogen (FG), a 340 kDa glycoprotein with concentrations in human plasma ranging from 1.5 to 3.5 mg/mL [40], is composed of three pairs of distinct polypeptide chains: α, β, and γ [41,42]. These chains are symmetrically organized into a trinodular structure featuring a central globular domain (E-domain) and two terminal globular domains (D-domains), connected by helical coiled-coil regions [43,44]. Additionally, FG possesses intrinsically disordered regions at the C-terminal ends of the α chains, known as αC regions, which confer structural flexibility and are essential for its interactions with other molecules [45,46]. The effects of FG on cells are mediated through integrin-based signaling pathways [47]. In bone, FG binding to αVβ3 integrin activates the expression of key differentiation genes in osteoblasts [48]. In addition, when prepared as a 3D porous scaffold and implanted in a critical bone defect model, FG supports the control of the initial immune response and bone repair/regeneration, with its complete biodegradation [49].

The present *in vitro* study aimed to investigate the effects of coating Nano-Ti with exogenous FG on the physicochemical properties of the surface and on the osteogenic differentiation of pre-osteoblastic cells. Our hypothesis was that the availability of FG on the nano-topographic Nano-Ti would enhance the osteogenic potential of cultures while also supporting the formation of a less inhomogeneous 3D fibrin fibril network when exposed to thrombin.

2. Material and methods

2.1. Preparation and functionalization of Nano-Ti surfaces

2.1.1. Preparation of Nano-Ti surfaces

To obtain the nano-topographic surface (Nano-Ti), commercially pure grade 2 Ti discs (Realum, São Paulo, SP, BR), with dimensions of 13 mm in width by 2 mm in thickness, were machined, sanded using silicon carbide papers of grits 150, 320, 600, and 1200, cleaned by sonication, and immersed in a solution consisting of equal volumes of 30 % H_2O_2 (107,210, Merck Millipore, Burlington, MA, USA) and concentrated H_2SO_4 (95–97 %, 100,731, Merck Millipore) for 2 h (10 mL/disc) at room temperature (≈ 25 °C) under constant agitation [18,19]. A significant exothermic reaction occurred during the initial phase of this process. At the end of the period, the discs were rinsed in distilled water, air-dried, and gamma-irradiated for sterilization with a dose of 25 kGy, corresponding to 2.5 Mrad of delivered energy (CETER – Radiation Technology Center at IPEN/CNEN/SP, São Paulo, SP, Brazil).

2.1.2. Coating of Nano-Ti surfaces with FG

On the same day as the cell culture experiments, FG coating (FG/Nano-Ti) – through simple adsorption – was performed on the surfaces of the Nano-Ti discs using bovine plasma FG protein (F8630, Sigma-Aldrich, St. Louis, MO, USA) in saline solution at 3 mg/mL. Briefly, the required amount of powder was weighed and diluted in 0.9 % NaCl solution under gentle agitation. The solution was then filtered through a 30 mm hydrophilic polyethersulfone (PES) membrane with 0.22 μm pores (Jet Biofil, Guangzhou, GD, China). The Nano-Ti discs were immersed in 1 mL of the solution and incubated for 2 h at 37 °C in a humidified atmosphere with 5 % CO_2 and 95 % atmospheric air [50].

2.2. Physicochemical characterization of Nano-Ti surfaces

2.2.1. BCA method for quantifying adsorbed FG

To quantify FG adsorbed by FG/Nano-Ti, the Pierce™ BCA Protein Assay Kit (Thermo Scientific - Thermo Fisher Scientific, Waltham, MA, USA) was used. The BCA (BiCinchoninic acid) protein quantification assay is based on the reduction of copper ions (Cu^{2+} to Cu^{+}) in an alkaline medium, followed by the formation of a purple complex between Cu^{+}

and BCA. After the coating process, the discs were scraped using 1000 μL pipette tips — using the fitting end — and the proteins were lysed with RIPA Lysis and Extraction Buffer (Thermo Scientific) and sonicated using an ultrasonic device (Misonix, Farmingdale, NY, USA). Nano-Ti was used as a negative control. For the colorimetric assay, following the manufacturer's instructions, the working solution was prepared by mixing Reagent A and Reagent B in a 50:1 ratio. Subsequently, 25 μL/well of each sample was deposited into 96-well plates (Corning Life Sciences, Tewksbury, MA, USA). Next, 200 μL/well of the working solution was added and incubated for 30 min at 37 °C. After the incubation period, the resulting solution was measured by colorimetric analysis in a spectrophotometer (562 nm, Epoch 2, BioTek Instruments Inc., Winooski, VT, USA). A standard curve, built with known concentrations of Bovine Serum Albumin (BSA - A7030, Sigma Aldrich), was used to calculate the protein concentration in the samples, ensuring high accuracy and sensitivity (20–2000 μg/mL).

2.2.2. Field emission scanning electron microscopy (FESEM)

The surface topography of the Nano-Ti and FG/Nano-Ti discs was observed using Field Emission Scanning Electron Microscopy (FESEM) with a GeminiSEM microscope (Carl Zeiss, Oberkochen, BW, Germany). Images were acquired at four different magnifications (10,000x, 50,000x, 100,000x, and 250,000x) with an electron acceleration voltage (EHT) set at 5 kV.

2.2.3. Kelvin probe force microscopy (KPFM)

The Kelvin Probe Force Microscopy (KPFM) technique measures the surface electric potential using a Bruker Innova KPFM microscope (Bruker, Billerica, MA, USA) equipped with a surface electric potential measurement tool. The equipment operated in lift mode: the forward scan captured topographic images in tapping mode, while the reverse scan acquired potential images in lift mode. To minimize artifacts, both the sample and the probe were grounded during the forward scan. In the reverse scan, the sample remained grounded while the probe was polarized. Nano-Ti samples were prepared with FG adsorbed only on part of the surface, allowing imaging (100 × 100 μm) at the interface between regions with and without FG to visualize the protein layer. All scans were conducted at a rate of 0.1 Hz (larger region) or 1 Hz (smaller region), with lift heights between 300 and 500 nm and an AC bias voltage of 3 V. Samples were measured under atmospheric air (humidity 35 ± 5 %). Images were processed using Gwyddion software [51].

2.2.4. Contact profilometer and confocal microscopy

To assess the surface roughness of Nano-Ti and FG/Nano-Ti, a contact profilometer (Intra Touch, Taylor Hobson Ltd., Leicester, LE, UK) and a laser scanning confocal microscope (LSM 900, Carl Zeiss) were employed. The confocal microscope provides greater precision at the nanometric scale, while the profilometer is more precise at the micrometric scale, making these techniques complementary [52]. Areas of 5 × 5 mm^2 were acquired with the contact profilometer, while 250 × 250 μm^2 areas were obtained with the confocal microscope. The images were tilt-corrected and filtered by applying a high-pass filter with a cutoff wavelength of 8 μm to remove waviness and a low-pass filter with a cutoff wavelength of 250 μm to capture roughness. Parameters of interest, such as arithmetic mean height (Sa), root mean square height (Sq), skewness (Ssk), and kurtosis (Sku) of the explored area, were extracted and expressed in μm in accordance with ISO 21,920–2021 and 25,178.

2.2.5. Zeta potential and dynamic light scattering (DLS)

Zeta potential titration curves of the FG solution were obtained using a Dynamic Light Scattering (DLS) instrument (Litesizer 500, Anton Paar, Graz, Styria, Austria). FG was dissolved in an electrolyte (1 mM KCl) to obtain a 3 mg/mL solution, as used for sample coating. The electrolyte was then buffered with HCl and NaOH solutions – both at 0.05 M – covering the pH range of 2.5 to 9. The Nano-Ti and FG/Nano-Ti discs were measured using an electrokinetic analyzer (SurPASS, Anton Paar). Using the adjustable-gap cell for discs, two samples of the same type were positioned parallel to each other, approximately 100 μm apart, and inserted into the instrument. The zeta potential was measured as a function of pH, while the electrolyte (1 mM KCl), buffered by an automatic titration unit with HCl and NaOH solutions – both at 0.05 M – circulated between the samples. Two different pairs of samples were used to evaluate the acidic (pH 2–5.5) and basic (pH 5.5–9) ranges, with the instrument being cleaned between measurements. The titration started at pH 5.5 for both pH ranges, with the automatic titration unit adding buffer solutions for 15 titration steps. For each pH value, three zeta potential measurements were taken, and the average was calculated.

2.2.6. Wettability

The Nano-Ti and FG/Nano-Ti surfaces were subjected to static wettability tests at room temperature (≈ 25 °C) by measuring the static contact angle using the sessile drop method [53]. Drops of 5 μL of distilled water, fetal bovine serum (FBS, Gibco), and blood, with γ ranging from 53 to 72 mN/m, were deposited on each surface, and their shapes were recorded using the DSA100E shape analyzer (KRÜSS, Hamburg, HH, Germany). The blood was collected at a clinical analysis laboratory and subsequently stored in the original sterile tube (BD Vacutainer K3E, 3S Healthcare, Devon, UK) containing 5.4 mg of ethylenediaminetetraacetic acid (EDTA), at a temperature between 2 °C and 6 °C (cooling bag with ice packs during transport/laboratory refrigerator). Contact angle measurements were performed in the same morning (and in any case within 5 days) after collection to minimize potential degradation. Before the experiment, the tube was gently agitated to homogenize the solution and allowed to reach room temperature. Contact angle measurements were then determined using the Drop Shape Analysis (DSA, KRÜSS) software, with three measurements performed on each sample, positioning the drops in different regions of the disc surface.

2.3. In vitro osteogenic differentiation

2.3.1. Culture of pre-osteoblastic cells

Pre-osteoblastic MC3T3-E1 cells, subclone 14 (ATCC CRL-2594, American Type Culture Collection, Manassas, VA, USA), were used. These cells were preserved in 2 mL cryogenic tubes in liquid nitrogen tanks, thawed, and cultured in 75 cm^2 flasks (Corning Life Sciences) containing 15 mL of α-MEM culture medium (Gibco, Thermo Fisher Scientific, Waltham, MA, USA) supplemented with 10 % FBS (Gibco) and streptomycin/penicillin at concentrations of 100 μg/mL and 100 IU/mL, respectively (Gibco). Throughout the culture period, cells were maintained at 37 °C in a humidified atmosphere containing 5 % CO_2 and 95 % atmospheric air, with media changes every two days. At subconfluence, cells were detached using 1 mM EDTA (Gibco) and 0.25 % trypsin (Gibco), then counted using an automated cell counter (Countess™ Automated Cell Counter, Invitrogen, Thermo Fisher Scientific, Carlsbad, *CA*, USA). Cells in suspension were plated directly onto Nano-Ti surfaces at densities of 2000 cells/disc for cellular morphology assays and 10,000 cells/disc for all other experiments. For cell culture, α-MEM medium supplemented with 10 % FBS, 100 μg/mL streptomycin, and 100 IU/mL penicillin was further enriched with 50 μg/mL ascorbic acid (50–81–7, Sigma-Aldrich) for the first 7 days. From day 8 to 18, 5 mM β-glycerophosphate (154,804–51–0, Sigma-Aldrich) was added. Cells were cultured under the atmospheric conditions described above throughout the entire period.

2.3.2. Cell morphology via epifluorescence

At 24 and 48 h, MC3T3-E1 cells were fixed with 4 % paraformaldehyde in 0.1 M phosphate buffer (PB, Sigma-Aldrich) for 10 min and washed three times in PB for 5 min each. Following washing, cultures were processed for direct fluorescence labeling [19] to visualize

the actin cytoskeleton and cell nuclei. Cells were permeabilized with 0.5 % Triton X-100 (Sigma-Aldrich) for 10 min. After washing in PB (3 ×, 5 min each), cells were incubated with Alexa Fluor 488-conjugated phalloidin (Molecular Probes, Thermo Fisher Scientific, Eugene, OR, USA) for 50 min, followed by additional PB washes. Nuclei were stained with 300 nM 4′,6-diamidino-2-phenylindole (DAPI, Molecular Probes) for 5 min, washed in distilled water, and mounted with glass coverslips using Fluoromount aqueous mounting medium (Sigma-Aldrich, Merck, St. Louis, MO, USA). Preparations were observed, and images were acquired using a Leica DM 4000 B fluorescence microscope equipped with a Leica DFC310 FX camera and Leica LAS X software.

2.3.3. Cell viability via live/dead assay

At 24 and 48 h, the viability of MC3T3-E1 cultures was qualitatively assessed using the LIVE/DEAD® Viability/Cytotoxicity Kit for mammalian cells (Molecular Probes), following the manufacturer's protocol. Live cells were stained green by intracellular esterase activity reacting with calcein (C30H26N2O13), while dead cells were stained red due to ethidium homodimer-1 (EthD-1) binding to nucleic acids. Images were captured using a Leica DM 4000 B fluorescence microscope equipped with a Leica DFC310 FX camera and Leica LAS X software.

2.3.4. Cell proliferation/viability via resazurin assay

On days 1, 3, and 5, cell proliferation/viability of MC3T3-E1 cultures was assessed via the resazurin reduction assay. This method measures the conversion of resazurin into a colorimetric end product (resorufin) by metabolically active cells. Non-viable cells lack this metabolic activity and do not produce a detectable signal [54]. Briefly, 10 μL of alamarBlue™ Cell Viability Reagent (Invitrogen) was diluted in 90 μL of supplemented culture medium, and 100 μL of this solution was added per well, followed by incubation at 37 °C for 4 h. Supernatants were then collected and transferred to 96-well plates for colorimetric measurement at 570 nm and 600 nm using a spectrophotometer (Epoch 2, BioTek Instruments Inc.).

2.3.5. Analysis of cellular differentiation via real-time polymerase chain reaction (Real-Time PCR)

At 7 days, the expression of genes related to osteogenic differentiation – transcription factor Runx2, alkaline phosphatase (Alp), osteopontin (Opn), bone sialoprotein (Bsp), osteoprotegerin (Opg), and osteocalcin (Oc) – was quantitatively assessed using the real-time PCR method. The sequences of the respective primers are presented in Table S1. Culture medium was removed from the wells, and Trizol LS reagent (Invitrogen) was added at room temperature (≈ 25 °C) for 5 min with agitation by pipetting. Total RNA extraction was performed using the SV Total RNA Isolation System kit (Promega, Madison, WI, USA), following the manufacturer's instructions. Subsequently, total RNA was quantified at different wavelengths (260, 280, 230, and 320 nm) using a spectrophotometer (GE Healthcare, Milwaukee, WI, USA). Following this, complementary DNA (cDNA) was synthesized from 1 μg of total RNA. This procedure was performed in a Mastercycle Gradient thermocycler (Eppendorf, Hamburg, Germany) using reverse transcriptase enzyme and the High-Capacity cDNA Reverse Transcription kit (Applied Biosystems, Thermo Fisher Scientific, Waltham, MA, USA). For real-time PCR reactions, specific primers (Sigma-Aldrich) with SYBR Green® detection were used for target genes, and reactions were carried out in a StepOne™ System apparatus (Applied Biosystems). Reactions were performed in technical quadruplicate using 5 μL of PowerUp™ SYBR™ Green Master Mix for qPCR (Applied Biosystems), 0.5 μL of forward primer (5′), 0.5 μL of reverse primer (3′), and 4 μL of cDNA (500 ng), resulting in a final reaction volume of 10 μL. Amplification cycles consisted of 2 min at 50 °C, 2 min at 95 °C, followed by 40 cycles of 3 s at 95 °C and 30 s at 60 °C (denaturation, annealing, and extension). Results were analyzed based on the Ct value (threshold cycle), defined as the cycle number where sample amplification crosses a threshold determined between the fluorescence level of negative controls and the exponential amplification phase of the samples, enabling quantitative analysis of the evaluated factor expression. β-actin (Actb) gene expression was used as an endogenous control for normalization of target gene expression levels. A negative sample (water) was subjected to reactions with each SYBR Green® probe used. The $2^{-\Delta\Delta Ct}$ method [55] was employed to compare gene expression between cultures grown on Nano-Ti and FG/Nano-Ti, assigning a value of 1 to each marker in cultures grown on Nano-Ti.

2.3.6. Analysis of cellular differentiation via protein expression using western blotting

At 7 days, the expression of proteins related to osteogenic differentiation – RUNX2, ALP, OPN, BSP, OPG, and OC – was evaluated using western blotting. For this, cells were detached from the disks by treatment with 0.25 % trypsin and 1 mM EDTA solution (Gibco), transferred to 15 mL Falcon tubes (Corning Life Sciences), and centrifuged at 2000 rpm for 5 min. After discarding the supernatant, the cell pellet was washed three times with 5 mL of pre-heated PBS (37 °C, Gibco). After the final centrifugation, PBS was removed, and the remaining cells were lysed with RIPA Lysis and Extraction Buffer (Thermo Scientific) and sonicated using ultrasound (Misonix). Briefly, the working solution was prepared by mixing reagents A and B in a 50:1 ratio, and subsequently, 25 μL/sample of each mixture was dispensed into 96-well plates (Corning Life Sciences). Then, 200 μL/well of the working solution was added, followed by incubation for 30 min at 37 °C. After the incubation period, the resulting solution was analyzed via colorimetry in a spectrophotometer (562 nm, Epoch 2, BioTek Instruments Inc.). Subsequently, 10 % acrylamide gels were prepared and mounted on appropriate supports, the tank was filled with running buffer, and wells were loaded with samples normalized to 30 μg protein per lane. Samples were heated at 95 °C for 5 min in a dry bath. Protein separation was performed by electrophoresis at 80 V for approximately 2 h using a molecular weight marker capable of identifying bands between 10 and 250 kDa (Bio-Rad, Hercules, *CA*, USA). Proteins were transferred from the gels to PVDF membranes with a 0.2 μm pore size (Bio-Rad) using the Trans-Blot® Turbo system (Bio-Rad) set to 25 V for 10 min. Membranes were subjected to three incubation steps: first, nonspecific binding sites were blocked with 5 % skim milk diluted in TBS-T buffer for 1 hour; second, membranes were incubated overnight with primary antibodies (Table S2); and third, membranes were incubated for 1 hour with HRP-conjugated secondary antibodies (1:2000, anti-rabbit IgG HRP #7074 or anti-mouse IgG HRP #7076; Cell Signaling Technology, Danvers, MA, USA). All primary and secondary antibodies were diluted according to the manufacturer's recommendations. After each incubation step, membranes were washed three times for 5 min with TBS-T buffer. Protein detection was performed by incubating the membranes for 1 min with Clarity™ Western ECL Substrate (Bio-Rad), and images were captured using the G:BOX system (SynGene, Cambridge, UK) with GeneSnap software (SynGene). Quantitative data of protein bands were obtained using the ImageJ software (NIH). Normalization of target protein expression was carried out relative to the constitutive protein glyceraldehyde-3-phosphate dehydrogenase (GAPDH), assigning a value of 1 to each marker in cultures on Nano-Ti. To achieve this, membranes were treated with *Re*-Blot Plus Strong Solution (Merck Millipore) for 20 min at room temperature (≈ 25 °C) to remove previous antibodies. Membranes were then re-incubated with the primary anti-GAPDH antibody (1:1000, rabbit polyclonal, Santa Cruz Biotechnology, Santa Cruz, *CA*, USA) and the HRP-conjugated secondary antibody (1:2000, Cell Signaling Technology), both diluted in 2.5 % skim milk in TBS-T.

2.3.7. In situ alkaline phosphatase (ALP) activity via the fast red method

Over a period of 7 and 10 days, an assay was conducted to visualize ALP activity *in situ*, using the Fast Red staining method [56]. The culture medium was removed, and the wells were washed with Hank's solution (Hank's Balanced Salts, Sigma-Aldrich) pre-warmed to 37 °C.

Subsequently, 1 mL/well of Tris buffer solution (Sigma-Aldrich) at 120 mM, pH 8.4, containing 1.8 mM Fast Red TR (Sigma-Aldrich), 0.9 mM naphthol-ASMX-phosphate (Sigma-Aldrich), and 1:9 dimethylformamide (Sigma-Aldrich, Merck) was added. The plates were then incubated for 30 min in a humidified atmosphere containing 5 % CO_2 and 95 % atmospheric air. The percentage of areas positively stained with Fast Red was determined from macroscopic images of the cultures grown on Nano-Ti and FG/Nano-Ti discs, digitally captured using a high-resolution camera (Canon EOS Digital Rebel T6i, 24.2 megapixels, equipped with an EF-S 18–55 mm macro lens, f/3.5–5.6 IS STM). These images were converted to binary format and analyzed by pixel quantification using ImageJ software (NIH). Qualitatively, Fast Red staining was also evaluated via epi-illumination fluorescence microscopy, using a Leica DM 4000 B microscope equipped with a Leica DFC310 FX camera and Leica LAS X software.

2.3.8. Detection of calcium content (Mineralized matrix formation) using alizarin red staining

At 14 and 18 days, the cultures were washed with Hank's solution (Sigma-Aldrich), fixed in 70 % ethanol at 4 °C for 1 hour, and then washed with PBS (Gibco) and double-distilled water. Subsequently, the samples were stained with 2 % Alizarin Red (Sigma-Aldrich), pH 4.2, at room temperature (≈ 25 °C) for 15 min, followed by washing with PBS and double-distilled water, and then dried at the same temperature. Macroscopic images of the cultures were digitally captured using a high-resolution camera (Canon EOS Digital Rebel T6i, 24.2 megapixels, equipped with an EF-S 18–55 mm macro lens, f/3.5–5.6 IS STM). Biochemical quantification of mineralization was performed using a colorimetric method [57]. After Alizarin Red staining, 360 μL of 10 % acetic acid were added to each well, and the plate was placed on a shaker for 30 min at room temperature (≈ 25 °C). The contents of each well were transferred to Eppendorf tubes, heated to 85 °C for 10 min, and then cooled on ice for 5 min. The tubes were centrifuged at 10,500 rpm for 15 min. Subsequently, 100 μL of the supernatant from each tube were transferred to a new tube. Then, 40 μL of 10 % ammonium hydroxide were added to neutralize the acid, and the entire content (140 μL) was transferred to a 96-well plate. Absorbance was measured using a spectrophotometer (405 nm; Epoch 2, BioTek Instruments Inc.). Qualitatively, Alizarin Red staining was also evaluated via epi-illumination fluorescence microscopy, using a Leica DM 4000 B microscope equipped with a Leica DFC310 FX camera and Leica LAS X software.

2.4. In vitro fibrin fiber formation

2.4.1. Scanning electron microscopy (SEM)

For fibrin network analysis, the discs were surface-coated with FG as previously described. After 2 h of coating, 1 IU of exogenous thrombin (T6634, Sigma-Aldrich), dissolved in 40 μL of 0.1 % (w/v) BSA solution (A7030, Sigma-Aldrich), was added to each disc. Following the 1 hour period required for polymerization, the discs were fixed with 3 % glutaraldehyde (112,179, Merck Millipore) diluted in 0.1 M phosphate buffer (Sigma-Aldrich). Subsequently, the samples were dehydrated in a graded ethanol series (30 %, 50 %, 70 %, 80 %, 95 %, and 100 %). Finally, the samples were sputter-coated and analyzed using a JSM-6610LV (JEOL Ltd., Akishima, Tokyo, Japan) or a Zeiss EVO-50XVP-BU (Carl Zeiss) scanning electron microscope. Images were acquired at different magnifications with an EHT set at 20 kV.

2.5. Data analysis

2.5.1. Statistical analysis

Quantitative data were subjected to normality and variance homogeneity tests. When the sample distribution showed normality and homoscedasticity, Student's *t*-test was applied to compare two groups; in cases of heteroscedasticity, the non-parametric Mann-Whitney test was used. For analyses involving two variation factors (group and time), two-way ANOVA and Tukey's post hoc test were applied. Statistical analyses were performed using the SigmaPlot 11.0 software (Systat Software Inc., San Jose, *CA*, USA), and the significance level was set at 5 % ($p < 0.05$).

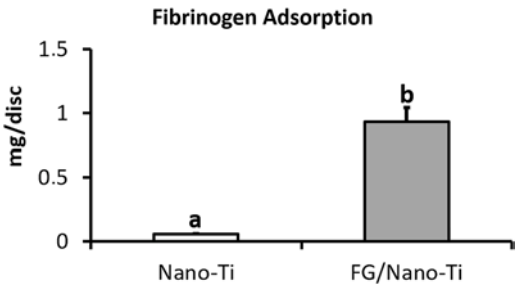


Fig. 1. Amount (mg/disc) of fibrinogen on nanostructured Ti surfaces either coated with fibrinogen (FG/Nano-Ti) or uncoated (Nano-Ti). Values are presented as mean ± standard deviation ($n = 3$). Distinct letters indicate statistical significance (Student's *t*-test, $p < 0.001$).

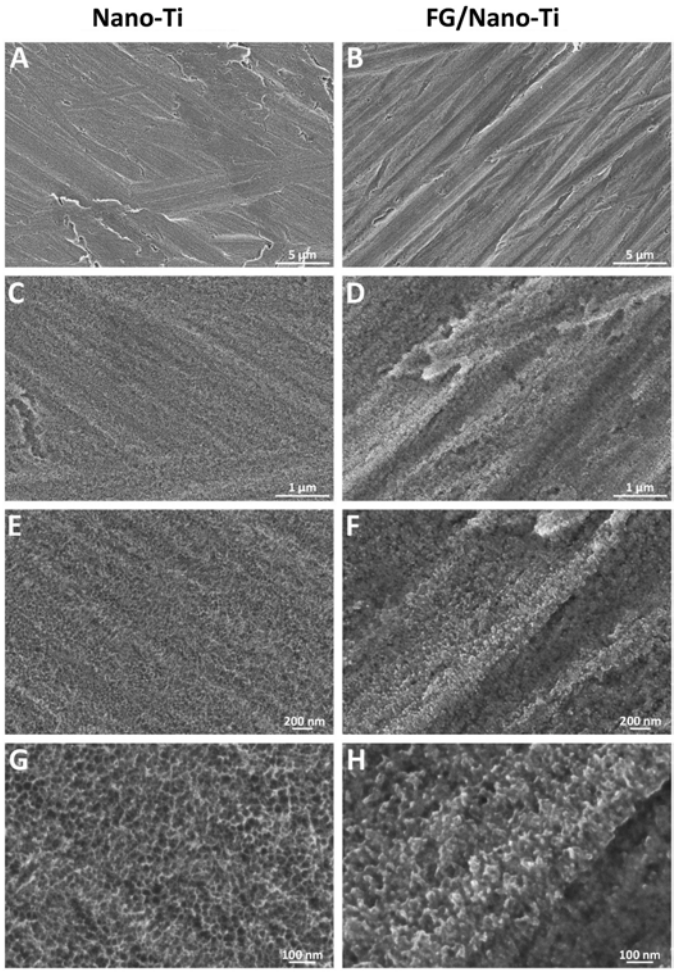


Fig. 2. Microscopic features observed by FESEM of nanostructured Ti surfaces (A-H), either coated with fibrinogen (B, D, F, and H) or uncoated (A, C, E, and G). Magnifications: 10,000x (A and B), 50,000x (C and D), 100,000x (E and F), and 250,000x (G and H).

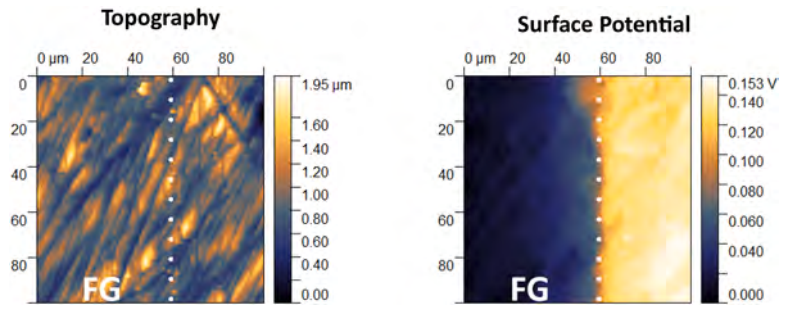


Fig. 3. Microscopic features observed by KPFM of a nanostructured Ti surface partially coated with fibrinogen (FG). On the left, the topography image with the fibrinogen boundary highlighted by dotted lines. On the right, is the surface electric potential image of the same region. Scanning area: 100 × 100 µm.

Table 1
Topographic parameters (mean ± standard deviation) – Sa and Sq (expressed in µm), and Ssk and Sku values – of nanostructured Ti surfaces, either coated with fibrinogen (FG/Nano-Ti) or uncoated (Nano-Ti), determined by contact profilometer and confocal microscope. The statistical significance of the difference between the two groups is reported (Student's *t*-test).

	Profilometer			Confocal Microscope		
	Nano-Ti	FG/Nano-Ti		Nano-Ti	FG/Nano-Ti	
Sa (µm)	0.15 ± 0.00	0.20 ± 0.02	$p < 0.05$	0.15 ± 0.02	0.19 ± 0.05	–
Sq (µm)	0.20 ± 0.01	0.27 ± 0.03	$p < 0.05$	0.20 ± 0.03	0.25 ± 0.05	–
Ssk	0.46 ± 0.11	1.22 ± 0.21	$p < 0.01$	0.59 ± 0.13	0.94 ± 0.07	$p < 0.05$
Sku	3.67 ± 0.27	4.81 ± 0.70	–	4.65 ± 0.42	5.25 ± 2.69	–

3. Results

3.1. Physicochemical characterization of Nano-Ti surfaces

3.1.1. Adsorbed FG

After coating, the FG/Nano-Ti discs exhibited approximately 0.7 mg/cm^2 of adsorbed FG on their nanostructured surface (0.93 mg normalized to the sample area – 1.3 cm^2). The uncoated discs showed negligible adsorption values (Student's *t*-test, $p < 0.001$; Fig. 1).

3.1.2. Scanning electron microscopy (FESEM)

Microscopic observations by FESEM revealed micro-grooves and nano-pores uniformly distributed in Nano-Ti and FG/Nano-Ti. The characteristic nanostructures of Nano-Ti, composed of a network of nanocavities, were found to be partially filled with nano-granular material exhibiting a relatively homogeneous distribution across the surface on FG/Nano-Ti (Fig. 2).

3.1.3. KPFM measurements

A specific sample was prepared for this technique, containing the reference uncoated surface (Nano-Ti) and the fibrinogen-coated surface (FG/Nano-Ti) on two separate areas of the same specimen. This allowed a reliable measure of the surface electric potential of the adsorbed layer *versus* the reference surface measured in the same experimental environment.

The topographic features revealed by KPFM showed that the adsorbed FG layer was not thick enough to mask the micro-grooves on Nano-Ti, resulting in a topographically indistinguishable protein layer (Fig. 3–

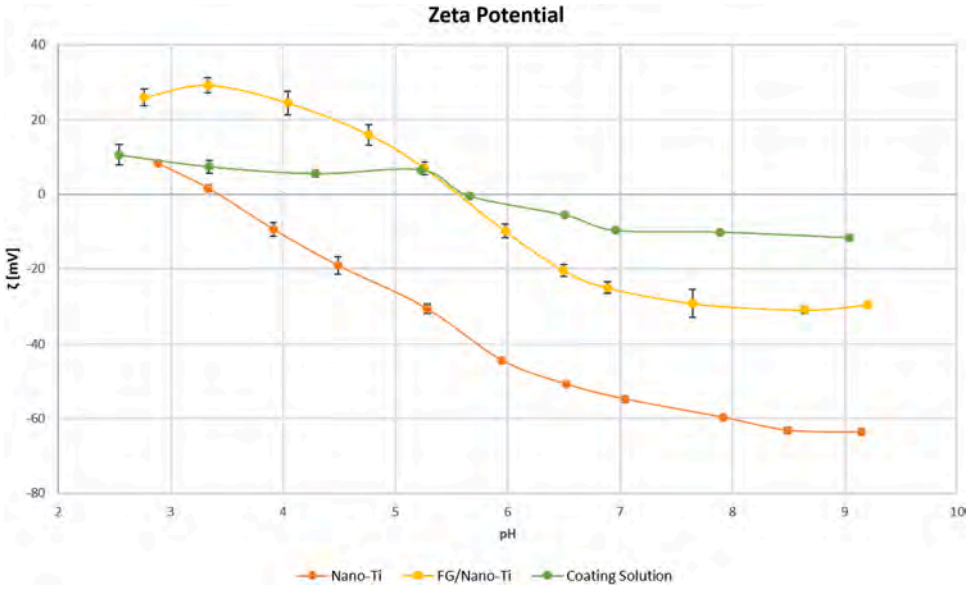


Fig. 4. Zeta potential titration curves for nanostructured Ti surfaces, either coated with fibrinogen (in yellow, FG/Nano-Ti) or uncoated (in orange, Nano-Ti), and for the coating solution (in green, DLS). Values are presented as mean ± standard deviation.

Table 2
Contact angles (mean ± standard deviation) for different fluids on nanostructured Ti surfaces, either coated with fibrinogen (FG/Nano-Ti) or uncoated (Nano-Ti). The statistical significance of the difference between the two groups is reported (Student's *t*-test).

Contact Angles			
	Nano-Ti	FG/Nano-Ti	
Deionized Water	24.87° ± 1.85	66.07° ± 0.25	$p < 0.01$
FBS	28.75° ± 0.35	34.80° ± 1.15	$p < 0.01$
Blood	108.00° ± 2.89	69.00° ± 2.77	$p < 0.01$

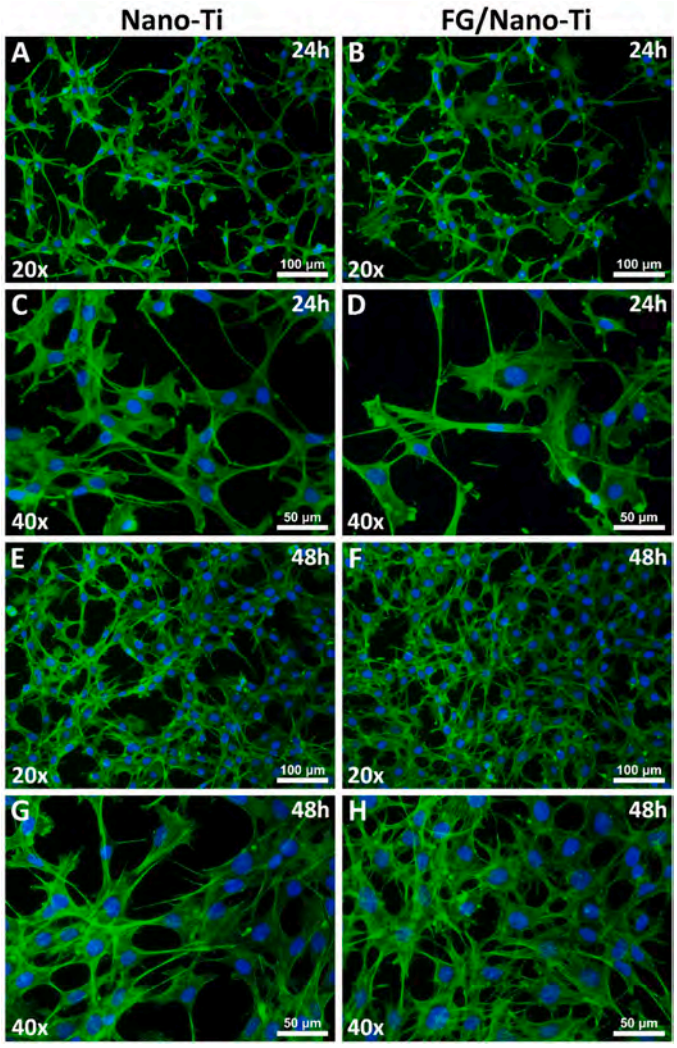


Fig. 5. Epifluorescence of MC3T3-E1 cells cultured on nanostructured Ti surfaces (A-H), either coated with fibrinogen (B, D, F, H - FG/Nano-Ti) or uncoated (A, C, E, G - Nano-Ti), after 24 (A-D) and 48 (E-H) hours. Blue fluorescence indicates cell nuclei, and green fluorescence, the actin cytoskeleton.

picture on the left and Fig. S3). On the contrary, a well-defined line was observed at the interface between the coated and uncoated regions when the electric surface potential was scanned, with an electric potential difference of approximately 80 mV (Fig. 3– picture on the right and Fig. S3).

3.1.4. Contact profilometer and confocal microscopy

Roughness measurements revealed a general tendency for higher values in FG/Nano-Ti, recorded both by the profilometer and the confocal microscope (Table 1, Fig. S4 and Fig. S5). Sa is the average

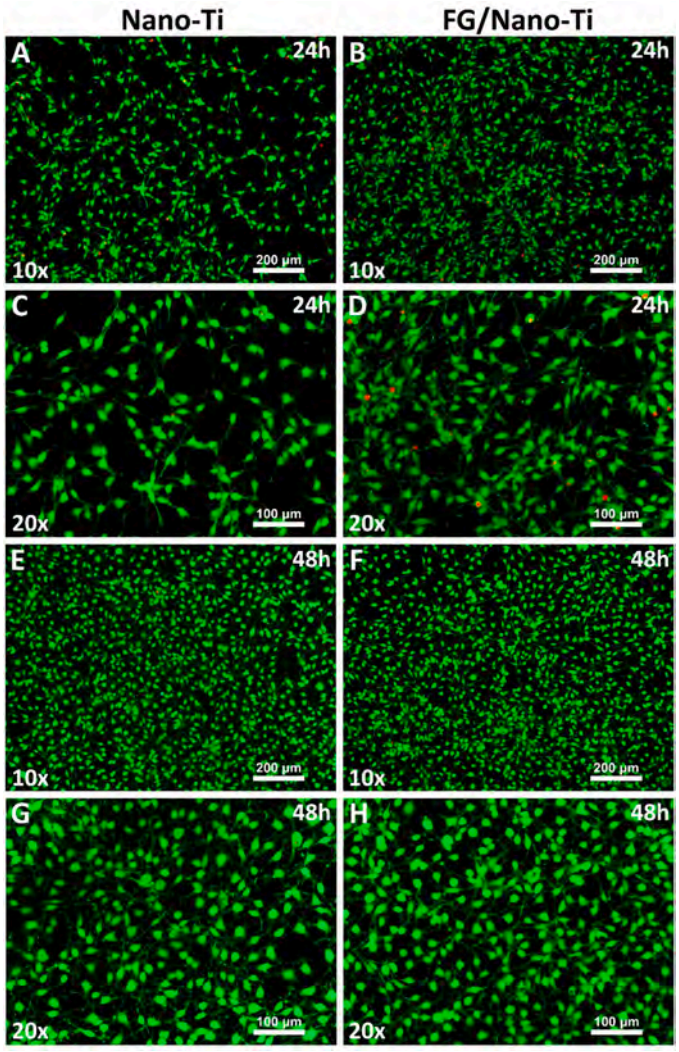


Fig. 6. Epifluorescence of MC3T3-E1 cells cultured on nanostructured Ti surfaces (A-H), either coated with fibrinogen (B, D, F, H - FG/Nano-Ti) or uncoated (A, C, E, G - Nano-Ti), after 24 (A-D) and 48 (E-H) hours. Green fluorescence indicates viable cells, and red fluorescence, dead cells.

roughness of a surface. Sq is the root mean square roughness with greater emphasis on extreme values: a ratio of Sa/Sq of 0.7 is expected for almost Gaussian surface features. Ssk is a measure of the symmetry of the surface profile as the balance between peaks and valleys; it is zero in the case of symmetry. Sku is a measure of the sharpness or flatness of the surface peaks and valleys: it is greater than 3 for a surface with sharp peaks and deep valleys, while less than 3 indicates a flatter surface, and 3 is expected for almost Gaussian surface features. Nano-Ti evidenced to be a surface with a sub-micrometric roughness (Sa and Sq around 0.15–0.20 µm), with a slight prevalence of surface peaks (Ssk>0) and almost Gaussian shape (Sa/Sq= 0.75; Sku around 4). Values of Sa, Sq, and Ssk measured by the contact profilometer were statistically higher on FG/Nano-Ti than on Nano-Ti and the confocal microscope confirmed the trend. No statistical difference was registered on Sku with values in the range of 3.8–5.2 for both surfaces.

3.1.5. Zeta potential titration curves and dynamic light scattering (DLS)

The zeta potential titration curves revealed distinct isoelectric points for Nano-Ti (3.5) and FG/Nano-Ti (5.5). The curve corresponding to the coated surface exhibited an isoelectric point similar to the FG (detected by DLS - Fig. 4). As a reference, the isoelectric point of Ti is 4. The curves of FG and FG/Nano-Ti show a distinct plateau for pH lower than 4 or

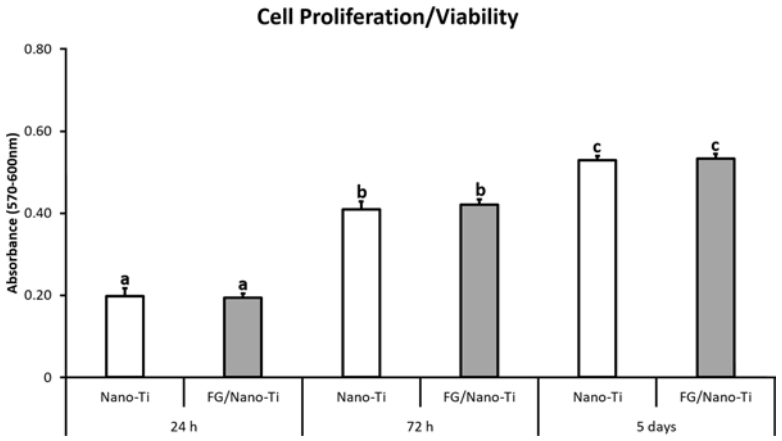


Fig. 7. Mean ± standard deviation values from the cell proliferation/viability assay in MC3T3-E1 pre-osteoblast cultures on nanostructured Ti surfaces, either coated with fibrinogen (FG/Nano-Ti) or uncoated (Nano-Ti), after 24 h, 72 h, and 5 days. Different letters indicate statistically significant differences (two-way ANOVA, $p < 0.001$) and same letters indicate no differences (two-way ANOVA, $p > 0.05$).

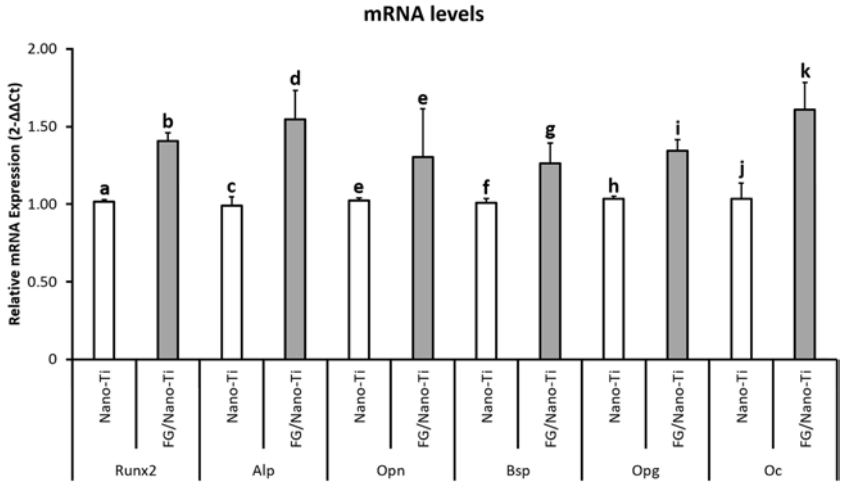


Fig. 8. Relative mRNA expression for Runx2, Alp, Opn, Bsp, Opg, and Oc at 7 days of culture of MC3T3-E1 pre-osteoblasts on nanostructured Ti surfaces, either coated with fibrinogen (FG/Nano-Ti) or uncoated (Nano-Ti). Values are presented as mean ± standard deviation. Different letters indicate statistically significant differences (Student's *t*-test, $p < 0.05$).

higher than 7.5. The curve of Nano-Ti shows a plateau only for pH higher than 8.5.

3.1.6. Wettability

Nano-Ti resulted in high hydrophilicity and it was also easily wetted by a drop of a protein medium such as FBS. The presence of FG reduced the hydrophilicity of the nano-topography when exposed to drops of either deionized water or FBS. In contrast, during interaction with blood, fibrinogen coating reduced the hydrophobicity of this surface (Table 2).

3.2. Biological results

3.2.1. Cell morphology

After 24 h, the cells were adherent and spread on Nano-Ti and FG/Nano-Ti surfaces. Most cells exhibited a polygonal morphology in a reticular arrangement, with multiple cytoplasmic processes extending in different directions, although some appeared more elongated. Bundles of F-actin stress fibers were distributed throughout the cytoplasm, extending to the cell boundaries (Fig. 5A–D). After 48 h, the morphological features remained similar, with a reduction in the number of elongated cells and a tendency for increased cell density on FG/Nano-Ti (Fig. 5E–H).

3.2.2. Cell viability

Epifluorescence images of MC3T3-E1 cultures stained with Live/Dead, obtained after 24 h, revealed adherent and spread cells, with a predominance of viable cells on both Nano-Ti and FG/Nano-Ti. An increase in cell density was also observed on FG/Nano-Ti (Fig. 6A–D). After 48 h, similar features of adhesion, spreading, viability, and cell density were observed (Fig. 6E–H).

3.2.3. Cell proliferation/viability

Cell proliferation values progressively increased over time on both surfaces (two-way ANOVA, $p < 0.001$). However, when comparing the groups, no statistically significant differences were observed (two-way ANOVA, $p > 0.05$; Fig. 7).

3.2.4. mRNA levels by quantitative real-time PCR

For all the markers evaluated, mRNA levels were significantly higher in MC3T3-E1 cultures grown on FG/Nano-Ti compared to Nano-Ti (Student's *t*-test, $p < 0.05$), with the exception of Opn, which showed only a trend toward higher expression (Fig. 8).

3.2.5. Protein levels by western blotting

The protein expression of the markers used was detected on both Nano-Ti and FG/Nano-Ti. The obtained values showed a greater

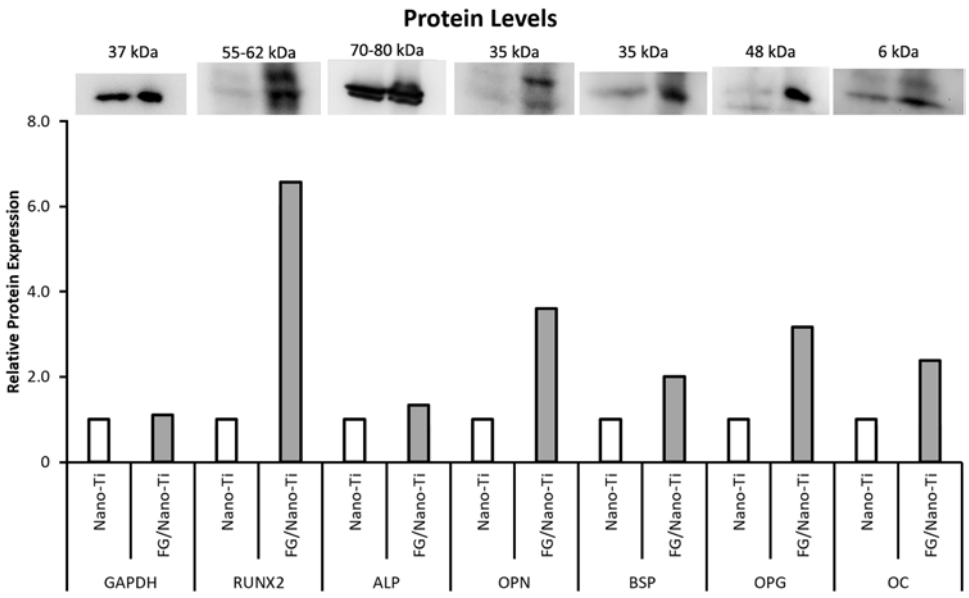


Fig. 9. Protein expression for RUNX2, ALP, OPN, BSP, OPG, and OC, normalized to GAPDH, at 7 days of culture of MC3T3-E1 pre-osteoblasts on nanostructured Ti surfaces, either coated with fibrinogen (FG/Nano-Ti) or uncoated (Nano-Ti).

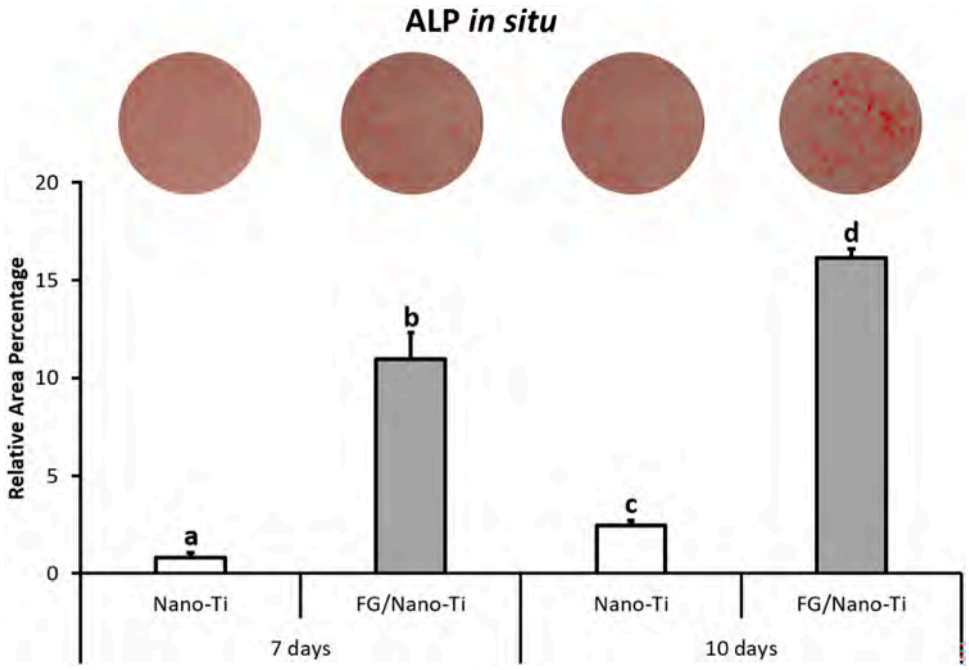


Fig. 10. Proportion of Fast Red-positive areas (*in situ* ALP activity) at 7 and 10 days of MC3T3-E1 pre-osteoblast cultures on nanostructured Ti surfaces, either coated with fibrinogen (FG/Nano-Ti) or uncoated (Nano-Ti). Values are presented as mean ± standard deviation. Different letters indicate statistically significant differences (two-way ANOVA, $p < 0.001$).

tendency for cultures grown on FG (Fig. 9).

3.2.6. *In situ alkaline phosphatase (ALP) activity*

The quantification of Fast Red-positive areas revealed higher *in situ* ALP activity in cultures grown in the presence of FG (7–10 days), compared to cultures grown on Nano-Ti (two-way ANOVA, $p < 0.001$; Fig. 10). When comparing time points, the cultures exhibited larger positive areas at 10 days for both surfaces (two-way ANOVA, $p < 0.001$; Fig. 10). Furthermore, microscopic images confirmed the presence of red fluorescence deposits, particularly in cultures grown on FG/Nano-Ti at both evaluated time points (Fig. 11).

3.2.7. *Calcium content detection (Mineralized matrix formation)*

Macroscopic observations using Alizarin Red staining revealed a diffuse mineral deposit pattern typically characteristic of MC3T3-E1 cultures on both Nano-Ti and FG/Nano-Ti surfaces (Fig. 12). Quantification showed greater mineralized matrix formation in cultures grown on FG (14–18 days) compared to cultures grown on Nano-Ti (two-way ANOVA, $p < 0.001$; Fig. 12). When comparing time points, the cultures exhibited larger positive areas at 18 days for both surfaces (two-way ANOVA, $p < 0.001$; Fig. 12). Epifluorescence images also revealed more intense positive staining, especially in cultures grown on FG/Nano-Ti at both time points evaluated (Fig. 13).

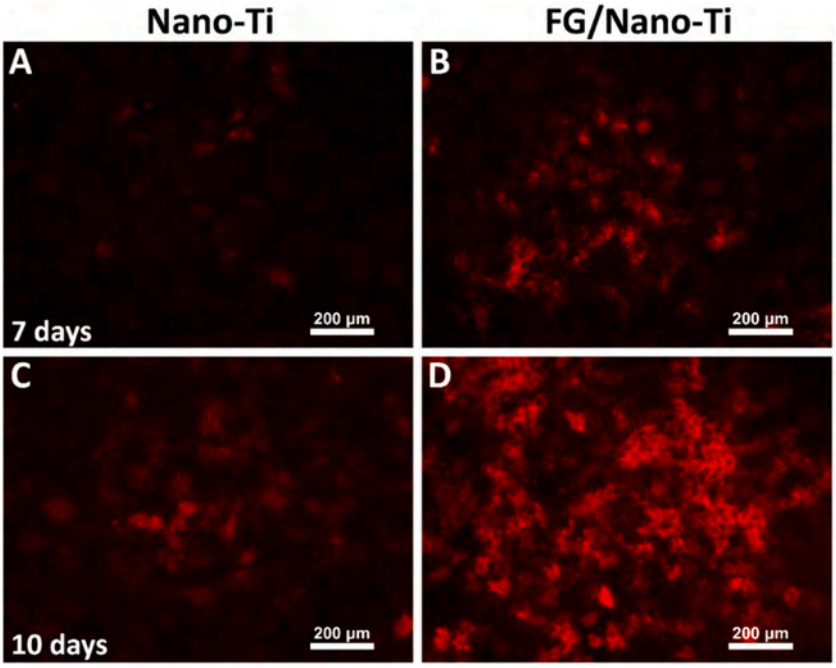


Fig. 11. Epifluorescence of Fast Red-positive areas (*in situ* ALP activity) at 7 and 10 days of MC3T3-E1 pre-osteoblast cultures on nanostructured Ti surfaces (A–D), either coated with fibrinogen (FG/Nano-Ti; B and D) or uncoated (Nano-Ti; A and C). Red fluorescence indicates positive staining for alkaline phosphatase.

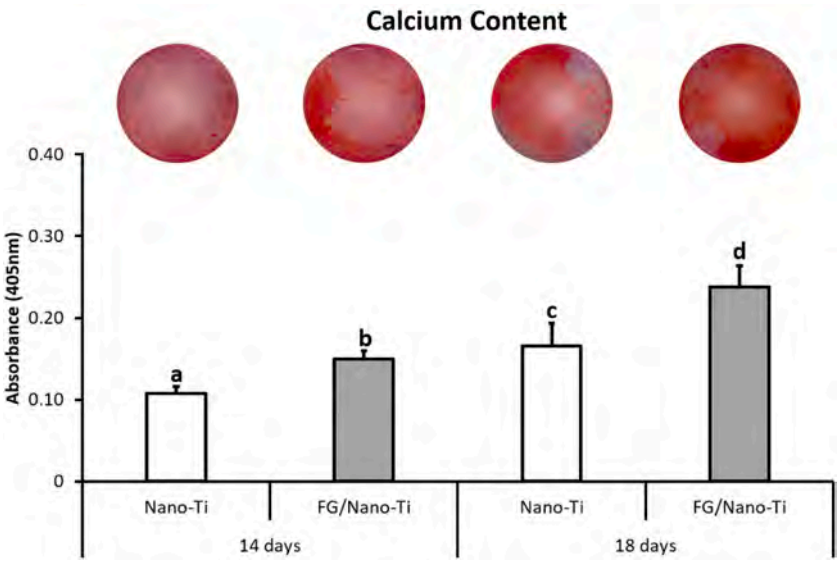


Fig. 12. Quantification of Alizarin Red staining by extraction at 14 and 18 days of MC3T3-E1 pre-osteoblast cultures on nanostructured Ti surfaces, either coated with fibrinogen (FG/Nano-Ti) or uncoated (Nano-Ti). Values are presented as mean ± standard deviation. Different letters indicate statistically significant differences (two-way ANOVA, $p < 0.001$).

3.3. In vitro fibrin fiber formation

Microscopic observations by SEM reveal the presence of fibrillar structures distributed across the entire surface of FG/Nano-Ti after the addition of exogenous thrombin. The formation of thin fibers structured as either delicate layers or regions with higher fibrillar density, with an interwoven, web-like pattern (Fig. 14). Coatings with 1 or 2 mg/mL FG resulted in areas that lacked fibrin fiber assembly (Fig. S1).

4. Discussion

In the present *in vitro* study, the surface coating of Nano-Ti with FG at its plasma concentration – 3 mg/mL –, close to a physiological condition, was evaluated regarding physicochemical characteristics, various biological response parameters in pre-osteoblastic cells, and the capacity to generate a homogeneous fibrin clot when exposed to thrombin. The rationale for using a solution of a single protein instead of a cocktail of different plasma proteins was to make the specific role of FG much more evident and to avoid interference due to the competition among different proteins. Morphologically, Nano-Ti and FG/Nano-Ti surfaces exhibited grooves at the micro-scale due to polishing (FESEM) (Fig. 2). The characteristic network of nanocavities of Nano-Ti due to etching was partially masked by the presence of nano-granulated material with a relatively homogeneous distribution over FG/Nano-Ti (FESEM) (Fig. 2).

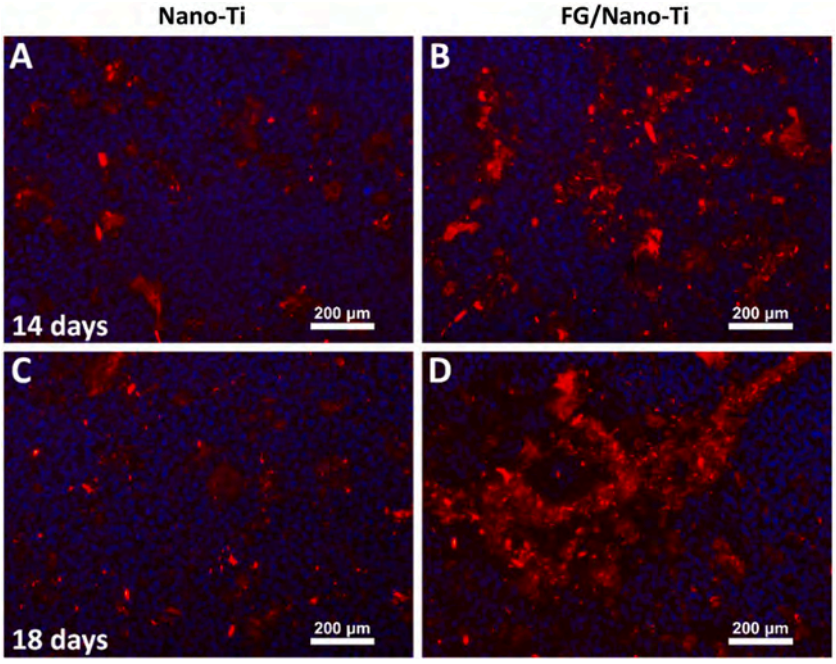


Fig. 13. Epifluorescence of Alizarin Red-stained areas at 14 and 18 days of MC3T3-E1 pre-osteoblast cultures on nanostructured Ti surfaces (A–D), either coated with fibrinogen (FG/Nano-Ti; B and D) or uncoated (Nano-Ti; A and C). Red fluorescence indicates positive Alizarin Red staining (calcium deposits) and blue fluorescence, cell nuclei.

In agreement with FESEM observations, roughness measurements by profilometry and confocal microscopy (Table 1) revealed a trend toward higher values for FG/Nano-Ti, possibly due to protein aggregate formation. KPFM revealed a continuous protein layer on FG/Nano-Ti which did not substantially change the surface topography, suggesting a submicrometric layer thickness (Fig. 3). This is relevant because a multiscale topography, with micro- and nano-features, is crucial to enhance cell adhesion and differentiation [58] and must not be masked by FG coating. The isoelectric point of the zeta potential titration curve of Nano-Ti evidenced the presence of some hydroxyl groups with an acidic reactivity because the isoelectric point is shifted to a lower value (3.5) than what was reported for Ti (4) (Fig. 4). During the adsorption of FG, the Nano-Ti surface is expected to be negatively charged with partially deprotonated hydroxyl groups. The titration curve of FG/Nano-Ti resembled that of the FG in solution (Fig. 4), confirming the presence of a continuous adsorbed protein layer with a tertiary configuration close to that in a water solution. The wettability measurements (Table 2) showed that Nano-Ti was highly hydrophilic and easily wettable by a protein medium. This is beneficial for osseointegration, which is reported to be higher for surfaces with a contact angle with water lower than 65° (Berg's limit) [59]. FG adsorption (FG/Nano-Ti) changed wettability (Table 2), confirming the presence of the adsorbed protein layer, with an increment of the water contact angle, as expected because of the presence of hydrophobic domains in FG. FG/Nano-Ti had a contact angle close to Berg's limit, within a range between 35° and 70°, and could thus be considered a moderately hydrophilic surface [60]. BCA results revealed that, on average, ≈ 0.9 mg of the FG in the solution was adsorbed onto FG/Nano-Ti (Fig. 1). The MC3T3-E1 cell culture results showed that osteogenic differentiation was enhanced on FG/Nano-Ti, with greater mRNA (Fig. 8) and protein expression (Fig. 9) of osteoblast markers, increased *in situ* ALP activity (Figs. 10 and Fig. 11), and more mineralized matrix formation (Figs. 12 and Fig. 13) in the cultures.

Despite the high wettability of Nano-Ti with water [9], the present study reveals that it is much less wettable when blood interacts with its surface (Table 2 and Fig. S2), a finding that could partially explain the inhomogeneity of blood clot on Nano-Ti *in vivo*, particularly that of its fibrin mesh network [27]. Indeed, hydrophobicity (contact angle > 90°) impairs the spreading of organic fluids – including blood – across biomaterial surfaces, negatively affecting a uniform coverage that potentially impacts on subsequent biological interactions [37]. In addition, host tissue factors such as (1) the complexity and irregularity of the blood vascular network at the implant site [61], (2) variations in blood viscosity depending on the type of ruptured blood vessels in the microcirculation – whether arterioles, capillaries, and/or venules [62], (3) the timing of blood coagulation depending on the extent of vascular injury and the amount of bleeding [63], and (4) the heterogeneity of blood clot contraction, resulting in variations in fibrin network thickness [34], would also contribute to the formation of inhomogeneous blood clot across the Nano-Ti and likely across other biomaterial surfaces. This led us to hypothesize that providing exogenous FG — at its plasma concentration — on Nano-Ti could potentially support the formation of a more homogeneous blood clot *in vivo*. The structural characteristics of blood clots have been considered crucial for optimal osseointegration of microtopographic Ti implant surfaces [28]. Interestingly, the wettability results using blood as a fluid revealed that FG/Nano-Ti reduced the contact angle by about 40° — from ≈ 110° to ≈ 70° — (Table 2 and Fig. S2), thus suggesting improved uniformity in initial blood spreading across its surface. In addition, by exposing FG/Nano-Ti to exogenous thrombin, a simple translational *in vitro* assay simulating the action of endogenous thrombin with blood extravasation at implant placement site, a thin gel layer with a macroscopic appearance resembling that of a fibrin network coating was formed [64]. Importantly, SEM imaging revealed the occurrence of fibrin fibril assembly throughout the entire FG/Nano-Ti surface (Fig.14), whereas the use of lower FG concentrations (1 or 2 mg/mL) for coating lacked areas of fibrin network (Fig. S1). As last, although Nano-Ti exhibits an osteogenic nano-topography, activating various signaling pathways [11–13,21,65], our approach of FG coating also benefits from the ability of FG to bind to αVβ3 integrin, stimulating the expression of osteoblast markers [48], and to bind to α9β1 integrin in undifferentiated stem cells, modulating Runx2 expression through the SMAD 1/5/8 signaling pathway [66].

The physicochemical characterization results are consistent with the fundamental role of Ti surface properties in its interaction with proteins [67,68]. The amount of FG adsorbed, equivalent to one-third of the

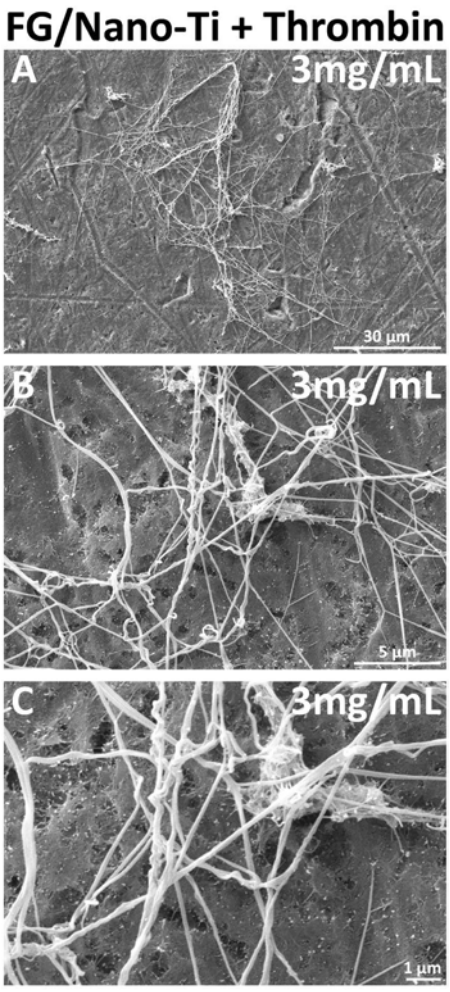


Fig. 14. SEM images of fibrin fibril assembly on a nanostructured Ti surface coated with fibrinogen (FG/Nano-Ti; A–C) after exposure to 1 IU thrombin for 1 h. Magnifications: 1,000x (A), 5,000x (B), and 10,000x (C).

solution used for coating (Fig. 1), was distributed as a thin, continuous layer on Nano-Ti (Figs. 3 and Fig. 4), reflecting the distribution and quantity of hydroxyl groups on this surface, which was considered reduced compared to other nano-topographies but enhanced with respect to Ti and its native oxide layer [69,70]. Accordingly, as evidenced by zeta potential titration curves (Fig. 4), the presence of deprotonated hydroxyl groups on Nano-Ti likely enhanced the electrostatic connection that is established with FG due to interactions with its positively charged αC terminal domains [71]. The size of a FG molecule on Ti is estimated to be 46 nm [72], which aligns with the observation that the nanopores, with an average diameter of approximately 20 nm [73], are only partially masked by the protein coating on FG/Nano-Ti (Fig. 2) – and not fully filled by the protein. Considering that topographic modifications of Ti surfaces allow for a higher initial release of coated proteins followed by smaller quantities in the subsequent days [74], FG/Nano-Ti likely supported a burst release of FG under our *in vitro* conditions.

FG/Nano-Ti had a relatively minimal impact on cell density during the first few days of culture (Figs. 5 and Fig. 6). The amount of FG adsorbed (0.7 mg/cm^2) is lower than concentrations of FG with recognized impact on substrate adhesion and proliferation (10–80 mg/mL in scaffold preparation or 4 mg/cm^2 for the higher concentration [75]), but much higher than levels that do not promote these events (10 µg/mL [76]). Despite that, the availability of endogenous thrombin to FG/Nano-Ti with the rupture of blood vessels at the site of implant placement could promote an enhancement in initial cell adhesion, migration and proliferation with the fibrin fibril assembly throughout its surface [77,78].

Although Nano-Ti's nano-topography, per se, already characterizes it as an osteogenic surface, it also offers the possibility of adsorption of molecules for eliciting specific biological responses. The results presented here showed increased osteogenic differentiation on FG/Nano-Ti, with a 1.5-fold increase in mRNA expression for Runx2 and Alp (Fig. 8), and 7- and 2-fold increases for RUNX2 and ALP proteins, respectively (Fig. 9). This had a positive impact on *in situ* ALP activity, between 7 and 14 times (Figs. 10 and Fig. 11), and on extracellular matrix (ECM) mineralization, with a 1.4-fold increase (Figs. 12 and Fig. 13), which aligns with the literature [66,79]. Additionally, the greater OPG production by MC3T3-E1 cells on FG/Nano-Ti (Figs. 8 and Fig. 9), along with the observation that FG has a binding site for the αMβ2 integrin of osteoclasts (discussed in [80]), indicates potential modulation of bone remodeling during the early post-implantation periods. Furthermore, as FG/Nano-Ti can be considered a moderately hydrophilic surface, the adsorption of FG should expose binding sites for the β2 integrin on macrophages, leading to M1 polarization, a pro-inflammatory state, through NF-κB activation [81], with potential impact on the formation of foreign body-type multinucleated giant cells and their functionality [82].

Taken together, the results presented in this work highlight the relevance of developing surface functionalization strategies for Ti with nano-topography using bioactive molecules. Particularly in the case of FG being made available on Nano-Ti through simple adsorption, significant biological effects were observed on a nano-topographic surface that has already been well recognized for its capacity to induce and promote osteogenic differentiation.

Author contributions

Antônio Secco Martorano was a PhD student in the Department of Oral Biology at the School of Dentistry of Ribeirão Preto, University of São Paulo (FORP-USP) and actively participated in all stages of the study, which is part of his doctoral thesis. Camilla Reggio contributed significantly to the physicochemical characterization assays, as well as to the experimental design, data processing, and critical revision of the manuscript. Luciana Oliveira de Almeida collaborated in the Western blot assays, data processing, and statistical analyses. Cristina Scolaro contributed with the wettability assay, interpretation of the results and discussion. Larissa Moreira Spinola de Castro Raucci played a key role in the study design, experimental execution, and critical revision of the manuscript. Silvia Spriano and Paulo Tambasco de Oliveira were involved in all phases of the study, from the initial planning to the completion of the research.

Funding

This study was financed in part by the Coordenação de Aperfeiçoamento de Pessoal de Nível Superior – Brasil (CAPES) – Finance Code 001, grant no. 88887.480303/2020–00; the Office of the Vice-Rectory for Graduate Studies – University of São Paulo (PRPG-USP), call no. 39/2022 (Santander Student Mobility Program); the São Paulo State Research Foundation (FAPESP, grant no. 2016/50298–4); and the National Council for Scientific and Technological Development (CNPq, grant no. 315266/2020–1).

Ethical approval

Ethical approval was not required because the experiments used ATCC's MC3T3-E1 subclone 14 cell line.

CRediT authorship contribution statement

Antônio Secco Martorano: Writing – review & editing, Writing – original draft, Visualization, Validation, Supervision, Software, Project administration, Methodology, Investigation, Formal analysis, Data curation, Conceptualization. **Camilla Reggio:** Writing – review & editing, Writing – original draft, Methodology, Investigation, Formal analysis, Data curation. **Luciana Oliveira de Almeida:** Writing – original draft, Methodology, Investigation, Formal analysis. **Cristina Scolaro:** Writing – original draft, Visualization, Validation, Methodology, Investigation, Formal analysis. **Larissa Moreira Spinola de Castro-Raucci:** Writing – original draft, Visualization, Methodology, Investigation, Formal analysis, Data curation. **Silvia Spriano:** Writing – review & editing, Writing – original draft, Supervision, Resources, Methodology, Investigation, Formal analysis, Data curation, Conceptualization. **Paulo Tambasco de Oliveira:** Writing – review & editing, Writing – original draft, Visualization, Validation, Supervision, Resources, Project administration, Methodology, Investigation, Funding acquisition, Data curation, Conceptualization.

Declaration of competing interest

The authors declare that they have no known competing financial interests or personal relationships that could have appeared to influence the work reported in this paper.

Acknowledgments

The authors would like to thank Lucas Dias de Oliveira, Roger Rodrigo Fernandes and Fabíola Singaretti de Oliveira for technical assistance during the cell culture and molecular biology experiments. Special thanks to José Augusto Maulim from the Central de Equipamentos e Serviços de Multiusuários (CESM), Ribeirão Preto Medical School – University of São Paulo (FMRP-USP), and Rodrigo Ferreira Silva from the Central Analítica da Química de Ribeirão Preto (CAQRP), Faculdade de Filosofia, Ciências e Letras de Ribeirão Preto – University of São Paulo (FFCLRP-USP), for their technical assistance with the scanning electron microscopy analyses.

Supplementary materials

Supplementary material associated with this article can be found, in the online version, at doi:10.1016/j.apsadv.2025.100837.

Data availability

Data will be made available on request.

References

[1] N. Hossain, M.A. Islam, M.M.S. Ahmed, M.A. Chowdhury, M.H. Mobarak, M. M. Rahman, M.H. Hossain, Advances and significances of titanium in dental implant applications, Results Chem 7 (2024) 101394, https://doi.org/10.1016/j.rechem.2024.101394.

[2] K. Harawaza, B. Cousins, P. Roach, A. Fernandez, Modification of the surface nanotopography of implant devices: a translational perspective, Mater. Today Bio 12 (2021) 100152, https://doi.org/10.1016/j.mtbio.2021.100152.

[3] J. Li, Y. Zheng, Z. Yu, R.K. Kankala, Q. Lin, J. Shi, C. Chen, K. Luo, A. Chen, Q. Zhong, Surface-modified titanium and titanium-based alloys for improved osteogenesis: a critical review, Heliyon. 10 (2024) e23779, https://doi.org/10.1016/j.heliyon.2023.e23779.

[4] Y. Zhang, Z. Fan, Y. Xing, S. Jia, Z. Mo, H. Gong, Effect of microtopography on osseointegration of implantable biomaterials and its modification strategies, Front. Bioeng. Biotechnol. 10 (2022) 981062, https://doi.org/10.3389/fbioe.2022.981062.

[5] G. Orsini, M. Piattelli, A. Scarano, G. Petrone, J. Kenealy, A. Piattelli, S. Caputi, Randomized, controlled histologic and histomorphometric evaluation of implants with nanometer-scale calcium phosphate added to the dual acid-etched surface in the human posterior maxilla, J. Periodontol. 78 (2007) 209–218, https://doi.org/10.1902/jop.2007.060297.

[6] N. Tsukimura, T. Ueno, F. Iwasa, H. Minamikawa, Y. Sugita, K. Ishizaki, T. Ikeda, K. Nakagawa, M. Yamada, T. Ogawa, Bone integration capability of alkali- and heat-treated nanobimorphic Ti-15Mo-5Zr-3Al, Acta Biomater 7 (2011) 4267–4277, https://doi.org/10.1016/j.actbio.2011.08.016.

[7] F. Variola, J.B. Brunski, G. Orsini, P. Tambasco de Oliveira, R. Wazen, A. Nanci, Nanoscale surface modifications of medically relevant metals: state-of-the art and perspectives, Nanoscale 3 (2011) 335–353, https://doi.org/10.1039/C0NR00485E.

[8] R.A. Gittens, R. Olivares-Navarrete, T. McLachlan, Y. Cai, S.L. Hyzy, J. M. Schneider, Z. Schwartz, K.H. Sandhage, B.D. Boyan, Differential responses of osteoblast lineage cells to nanotopographically-modified, microroughened titanium-aluminum-vanadium alloy surfaces, Biomaterials 33 (2012) 8986–8994, https://doi.org/10.1016/j.biomaterials.2012.08.059.

[9] P.T. de Oliveira, S.F. Zalzal, M.M. Beloti, A.L. Rosa, A. Nanci, Enhancement of in vitro osteogenesis on titanium by chemically produced nanotopography, J. Biomed. Mater. Res. A 80 (2007) 554–564, https://doi.org/10.1002/jbm.a.30955.

[10] C.J. Bettinger, R. Langer, J.T. Borenstein, Engineering substrate topography at the micro- and nanoscale to control cell function, Angew. Chem. Int. Ed. 48 (2009) 5406–5415, https://doi.org/10.1002/anie.200805179.

[11] L.M.S. Castro-Raucci, M.S. Francischini, L.N. Teixeira, E.P. Ferraz, H.B. Lopes, P. T. de Oliveira, M.Q. Hassan, A.L. Rosa, M.M. Beloti, Titanium with nanotopography induces osteoblast differentiation by regulating endogenous bone morphogenetic protein expression and signaling pathway, J. Cell. Biochem. 117 (2016) 1718–1726, https://doi.org/10.1002/jcb.25469.

[12] R.P.F. Abuna, F.S. Oliveira, H.B. Lopes, G.P. Freitas, R.R. Fernandes, A.L. Rosa, M. M. Beloti, The Wnt/β-catenin signaling pathway is regulated by titanium with nanotopography to induce osteoblast differentiation, Colloids. Surf. B Biointerfaces. 184 (2019) 110513, https://doi.org/10.1016/j.colsurfb.2019.110513.

[13] H.B. Lopes, G.P. Freitas, D.M.C. Fantacini, V. Picanço-Castro, D.T. Covas, A.L. Rosa, M.M. Beloti, Titanium with nanotopography induces osteoblast differentiation through regulation of integrin αV, J. Cell. Biochem. 120 (2019) 16723–16732, https://doi.org/10.1002/jcb.28930.

[14] D.Guadarrama Bello, A. Fouillen, A. Badia, A. Nanci, Nanoporosity stimulates cell spreading and focal adhesion formation in cells with mutated paxillin, ACS Appl. Mater. Interfaces 12 (2020) 14924–14932, https://doi.org/10.1021/acsami.0c01172.

[15] J. Luo, M. Walker, Y. Xiao, H. Donnelly, M.J. Dalby, M. Salmeron-Sanchez, The influence of nanotopography on cell behaviour through interactions with the extracellular matrix – A review, Bioact. Mater. 15 (2022) 145–159, https://doi.org/10.1016/j.bioactmat.2021.11.024.

[16] R.L. Bighetti-Trevisan, L.O. Almeida, L.M.S. Castro-Raucci, J.A.R. Gordon, C. E. Tye, G.S. Stein, J.B. Lian, J.L. Stein, A.L. Rosa, M.M. Beloti, Titanium with nanotopography attenuates the osteoclast-induced disruption of osteoblast differentiation by regulating histone methylation, Biomater. Adv. 134 (2022) 112548, https://doi.org/10.1016/j.msec.2021.112548.

[17] R.L. Bighetti-Trevisan, E.P. Ferraz, M.B.F. Silva, G.C. Zatta, M.B. de Almeida, A. L. Rosa, M.M. Beloti, Effect of osteoblasts on osteoclast differentiation and activity induced by titanium with nanotopography, Colloids. Surf. B Biointerfaces. 229 (2023) 113448, https://doi.org/10.1016/j.colsurfb.2023.113448.

[18] A. Nanci, J.D. Wuest, L. Peru, P. Brunet, V. Sharma, S. Zalzal, M.D. McKee, Chemical modification of titanium surfaces for covalent attachment of biological molecules, J. Biomed. Mater. Res. 40 (1998) 324–335. https://onlinelibrary.wiley.com/doi/10.1002/(SICI)1097-4636(199805)40:2<324::AID-JBM18>3.0.CO;2-L.

[19] P.T. de Oliveira, A. Nanci, Nanotexturing of titanium-based surfaces upregulates expression of bone sialoprotein and osteopontin by cultured osteogenic cells, Biomaterials 25 (2004) 403–413, https://doi.org/10.1016/s0142-9612(03)00539-8.

[20] D.Guadarrama Bello, A. Fouillen, A. Badia, A. Nanci, A nanoporous titanium surface promotes the maturation of focal adhesions and formation of filopodia with distinctive nanoscale protrusions by osteogenic cells, Acta Biomater 60 (2017) 339–349, https://doi.org/10.1016/j.actbio.2017.07.022.

[21] R.B. Kato, B. Roy, F.S. de Oliveira, E.P. Ferraz, P.T. de Oliveira, A.G. Kemper, M. Q. Hassan, A.L. Rosa, M.M. Beloti, Nanotopography directs mesenchymal stem cells to osteoblast lineage through regulation of microRNA-SMAD-BMP-2 circuit, J. Cell. Physiol. 229 (2014) 1690–1696, https://doi.org/10.1002/jcp.24614.

[22] R.M. Wazen, S. Kuroda, C. Nishio, K. Sellin, J.B. Brunski, A. Nanci, Gene expression profiling and histomorphometric analyses of the early bone healing response around nanotextured implants, Nanomedicine (Lond.) 8 (2013) 1385–1395, https://doi.org/10.2217/nnm.12.167.

[23] S. Ferraris, M. Cazzola, L.R. Zuardi, P.T. de Oliveira, Metal nanoscale systems functionalized with organic compounds. Nanostructured Biomaterials for Regenerative Medicine, Woodhead Publishing, Cambridge, 2020, pp. 407–436, https://doi.org/10.1016/B978-0-08-102594-9.00015-2.

[24] D. Rana, K. Ramasamy, M. Leena, R. Pasricha, G. Manivasagam, M. Ramalingam, Surface functionalization of biomaterials. Biological Engineering of Stem Cell Niches, Elsevier, Cambridge, 2017, pp. 331–343, https://doi.org/10.1016/B978-0-12-802734-9.00021-4.

[25] J.D. Malcor, F. Mallein-Gerin, Biomaterial functionalization with triple-helical peptides for tissue engineering, Acta Biomater 148 (2022) 1–21, https://doi.org/10.1016/j.actbio.2022.06.003.

[26] H.T. Shiu, B. Goss, C. Lutton, R. Crawford, Y. Xiao, Formation of blood clot on biomaterial implants influences bone healing, Tissue Eng. Part B Rev. 20 (2014) 697–712, https://doi.org/10.1089/ten.TEB.2013.0709.

[27] L.R. Zuardi, C.L.A. Silva, E.M. Rego, G.V. Carneiro, S. Spriano, A. Nanci, P.T. de Oliveira, Influence of a physiologically formed blood clot on pre-osteoblastic cells grown on a BMP-7-coated nanoporous titanium surface, Biomimetics. (Basel) 8 (2023) 123, https://doi.org/10.3390/biomimetics8010123.

[28] D. Di Iorio, T. Traini, M. Degidi, S. Caputi, J. Neugebauer, A. Piattelli, Quantitative evaluation of the fibrin clot extension on different implant surfaces: an in vitro study, J. Biomed. Mater. Res. B Appl. Biomater. 74 (2005) 636–642, https://doi.org/10.1002/jbm.b.30251.

[29] Y. Cui, Y. Yang, D. Qiu, Design of selective cell migration biomaterials and their applications for tissue regeneration, J. Mater. Sci. 56 (2021) 4080–4096, https://doi.org/10.1007/s10853-020-05537-y.

[30] V. Milleret, S. Tugulu, F. Schlottig, H. Hall, Alkali treatment of microrough titanium surfaces affects macrophage/monocyte adhesion, platelet activation and architecture of blood clot formation, Eur. Cell Mater. 21 (2011) 430–444, https://doi.org/10.22203/ecm.v021a32.

[31] J. Li, J. Zhao, Y. Xu, A. Xu, F. He, Titanium surface interacting with blood clot enhanced migration and osteogenic differentiation of bone marrow mesenchymal stem cells, Front. Bioeng. Biotechnol. 11 (2023) 1136406, https://doi.org/10.3389/fbioe.2023.1136406.

[32] H.H. Huang, Z.H. Chen, D.T. Nguyen, C.M. Tseng, C.S. Chen, J.H. Chang, Blood coagulation on titanium dioxide films with various crystal structures on titanium implant surfaces, Cells 11 (2022) 2623, https://doi.org/10.3390/cells11172623.

[33] T. Traini, G. Murmura, B. Sinjari, G. Perfetti, A. Scarano, C. D'Arcangelo, S. Caputi, The surface anodization of titanium dental implants improves blood clot formation followed by osseointegration, Coatings 8 (2018) 252, https://doi.org/10.3390/coatings8070252.

[34] Y. Zou, Z. Shan, Z. Han, J. Yang, Y. Lin, Z. Gong, L. Xie, J. Xu, R. Xie, Z. Chen, Z. Chen, Regulating blood clot fibrin films to manipulate biomaterial-mediated foreign body responses, Res. (Wash. D.C.) 6 (2023) 0225, https://doi.org/10.34133/research.0225.

[35] M. Jalaluddin, P.K. Ramanna, M. Swain, S. Sonkesriya, P. Rana, D. Kumari, D.A. A. Derbala, L.F. Mirza, S. Mushtaq, S.E.M. Beshir, Evaluation of fibrin clot interaction with dental implant after different surface treatments: an *in vitro* study, J. Contemp. Dent. Pract. 25 (2024) 276–279, https://doi.org/10.5005/jp-journals-10024-3653.

[36] J. Hong, J. Andersson, K.N. Ekdahl, G. Elgue, N. Axén, R. Larsson, B. Nilsson, Titanium is a highly thrombogenic biomaterial: possible implications for osteogenesis, Thromb. Haemost. 82 (1999) 58–64, https://doi.org/10.1055/s-0037-1614630.

[37] B.S. Kopf, S. Ruch, S. Berner, N.D. Spencer, K. Maniura-Weber, The role of nanostructures and hydrophilicity in osseointegration: In-vitro protein-adsorption and blood-interaction studies, J. Biomed. Mater. Res. A 103 (2015) 2661–2672, https://doi.org/10.1002/jbm.a.35401.

[38] J. Yang, Y. Zhou, F. Wei, Y. Xiao, Blood clot formed on rough titanium surface induces early cell recruitment, Clin. Oral Implants Res. 27 (2016) 1031–1038, https://doi.org/10.1111/clr.12672.

[39] T.A. Horbett, Fibrinogen adsorption to biomaterials, J. Biomed. Mater. Res. a 106 (2018) 2777–2788, https://doi.org/10.1002/jbm.a.36460.

[40] R.I. Litvinov, J.W. Weisel, What is the biological and clinical relevance of fibrin? Semin. Thromb. Hemost. 42 (2016) 333–343, https://doi.org/10.1055/s-0036-1571342.

[41] S. Herrick, O. Blanc-Brude, A. Gray, G. Laurent, Fibrinogen, Int. J. Biochem. Cell Biol. 31 (1999) 741–746, https://doi.org/10.1016/s1357-2725(99)00032-1.

[42] J.W. Weisel, Fibrinogen and fibrin, Adv. Protein Chem. 70 (2005) 247–299, https://doi.org/10.1016/S0065-3233(05)70008-5.

[43] H.R. Millar, J.G. Simpson, A.L. Stalker, An evaluation of the heat precipitation method for plasma fibrinogen estimation, J. Clin. Pathol. 24 (1971) 827–830, https://doi.org/10.1136/jcp.24.9.827.

[44] N.A. Barinov, A.D. Protopopova, E.V. Dubrovin, D.V. Klinov, Thermal denaturation of fibrinogen visualized by single-molecule atomic force microscopy, Colloids Surf. B Biointerfaces 167 (2018) 370–376, https://doi.org/10.1016/j.colsurfb.2018.04.037.

[45] M.W. Mosesson, Fibrinogen and fibrin structure and functions, J. Thromb. Haemost. 3 (2005) 1894–1904, https://doi.org/10.1111/j.1538-7836.2005.01365.x.

[46] A.S. Wolberg, Fibrinogen and fibrin: synthesis, structure, and function in health and disease, J. Thromb. Haemost. 21 (2023) 3005–3015, https://doi.org/10.1016/j.jtha.2023.08.014.

[47] X. Pang, X. He, Z. Qiu, H. Zhang, R. Xie, Z. Liu, Y. Gu, N. Zhao, Q. Xiang, Y. Cui, Targeting integrin pathways: mechanisms and advances in therapy, Signal Transduct. Target. Ther. 8 (2023) 1, https://doi.org/10.1038/s41392-022-01259-6.

[48] M.C. Siebers, P.J. ter Brugge, X.F. Walboomers, J.A. Jansen, Integrins as linker proteins between osteoblasts and bone replacing materials: a critical review, Biomaterials 26 (2005) 137–146, https://doi.org/10.1016/j.biomaterials.2004.02.021.

[49] D.M. Vasconcelos, R.M. Gonçalves, C.R. Almeida, I.O. Pereira, M.I. Oliveira, N. Neves, A.M. Silva, A.C. Ribeiro, C. Cunha, A.R. Almeida, C.C. Ribeiro, A.M. Gil, E. Seebach, K.L. Kynast, W. Richter, M. Lamghari, S.G. Santos, M.A. Barbosa, Fibrinogen scaffolds with immunomodulatory properties promote in vivo bone regeneration, Biomaterials 111 (2016) 163–178, https://doi.org/10.1016/j.biomaterials.2016.10.004.

[50] J. Barberi, S. Ferraris, A.M. Giovannozzi, L. Mandrile, E. Piatti, A.M. Rossi, S. Spriano, Advanced characterization of albumin adsorption on a chemically treated surface for osseointegration: an innovative experimental approach, Mater. Des. 218 (2022) 110712, https://doi.org/10.1016/j.matdes.2022.110712.

[51] D. Nečas, P. Klapetek, Gwyddion: an open-source software for SPM data analysis, Open Phys 10 (2012) 181–188, https://doi.org/10.2478/s11534-011-0096-2.

[52] V.A. Gobbo, M. Lallukka, F. Gamna, M. Prato, A. Vitale, S. Ferraris, Z. Najmi, A. Cochis, L. Rimondini, J. Massera, S. Spriano, Functionalization of a chemically treated Ti6Al4V-ELI alloy with nisin for antibacterial purposes, Appl. Surf. Sci. 620 (2023) 156820, https://doi.org/10.1016/j.apsusc.2023.156820.

[53] A.W. Adamson, A.P. Gast, The solid–liquid interface-contact angle, in: A. W. Adamson, A.P. Gast (Eds.), Physical Chemistry of Surfaces, John Wiley & Sons Inc., New York, 1997, pp. 347–389.

[54] J.L. Chen, T.W.J. Steele, D.C. Stuckey, Metabolic reduction of resazurin; location within the cell for cytotoxicity assays, Biotechnol. Bioeng. 115 (2018) 351–358, https://doi.org/10.1002/bit.26475.

[55] K.J. Livak, T.D. Schmittgen, Analysis of relative gene expression data using real-time quantitative PCR and the 2(–Delta Delta C(T)) method, Methods 25 (2001) 402–408, https://doi.org/10.1006/meth.2001.1262.

[56] A.K. Majors, C.A. Boehm, H. Nitto, R.J. Midura, G.F. Muschler, Characterization of human bone marrow stromal cells with respect to osteoblastic differentiation, J. Orthop. Res. 15 (1997) 546–557, https://doi.org/10.1002/jor.1100150410.

[57] C.A. Gregory, W.G. Gunn, A. Peister, D.J. Prockop, An Alizarin red-based assay of mineralization by adherent cells in culture: comparison with cetylpyridinium chloride extraction, Anal. Biochem. 329 (2004) 77–84, https://doi.org/10.1016/j.ab.2004.02.002.

[58] S. Tuikampee, P. Chaijareenont, P. Rungsiyakull, A. Yavirach, Titanium surface modification techniques to enhance osteoblasts and bone formation for dental implants: A narrative review on current advances, Metals 14 (2024) 515, https://doi.org/10.3390/met14050515.

[59] T. Mekayarajjananonth, S. Winkler, Contact angle measurement on dental implant biomaterials, J. Oral Implantol. 25 (1999) 230–236, https://doi.org/10.1563/1548-1336(1999)025<0230:CAMODI>2.3.CO;2.

[60] E.J. Falde, S.T. Yohe, Y.L. Colson, M.W. Grinstaff, Superhydrophobic materials for biomedical applications, Biomaterials 104 (2016) 87–103, https://doi.org/10.1016/j.biomaterials.2016.06.050.

[61] C. O'Connor, E. Brady, Y. Zheng, E. Moore, K.R. Stevens, Engineering the multiscale complexity of vascular networks, Nat. Rev. Mater. 7 (2022) 702–716, https://doi.org/10.1038/s41578-022-00447-8.

[62] A.S. Popel, P.C. Johnson, Microcirculation and hemorheology, Annu Rev. Fluid. Mech. 37 (2005) 43–69, https://doi.org/10.1146/annurev.fluid.37.042604.133933.

[63] A.Y. Mitrophanov, G. Merrill-Skoloff, S.P. Grover, V. Govindarajan, A. Kolanjiyil, D.S. Hariprasad, G. Unnikrishnan, R. Flaumenhaft, J. Reifman, Injury length and arteriole constriction shape clot growth and blood-flow acceleration in a mouse model of thrombosis, Arterioscler. Thromb. Vasc. Biol. 40 (2020) 2114–2126, https://doi.org/10.1161/ATVBAHA.120.314786.

[64] P.A. Janmey, J.P. Winer, J.W. Weisel, Fibrin gels and their clinical and bioengineering applications, J. R. Soc. Interface 6 (2009) 1–10, https://doi.org/10.1098/rsif.2008.0327.

[65] A.L. Rosa, R.B. Kato, L.M. Castro Raucci, L.N. Teixeira, F.S. de Oliveira, L. S. Bellesini, P.T. de Oliveira, M.Q. Hassan, M.M. Beloti, Nanotopography drives stem cell fate toward osteoblast differentiation through α1β1 integrin signaling pathway, J. Cell. Biochem. 115 (2014) 540–548, https://doi.org/10.1002/jcb.24688.

[66] F. Kidwai, J. Edwards, L. Zou, D.S. Kaufman, Fibrinogen induces RUNX2 activity and osteogenic development from human pluripotent stem cells, Stem Cells 34 (2016) 2079–2089, https://doi.org/10.1002/stem.2427.

[67] J. Barberi, S. Spriano, Titanium and protein adsorption: an overview of mechanisms and effects of surface features, Materials (Basel) 14 (2021) 1590, https://doi.org/10.3390/ma14071590.

[68] T. Matsumoto, Y. Tashiro, S. Komasa, A. Miyake, Y. Komasa, J. Okazaki, Effects of surface modification on adsorption behavior of cell and protein on titanium surface by using quartz crystal microbalance system, Materials (Basel) 14 (2021) 97, https://doi.org/10.3390/ma14010097.

[69] S. Ferraris, A. Bobbio, M. Miola, S. Spriano, Micro- and nano-textured, hydrophilic and bioactive titanium dental implants, Surf. Coat. Technol. 276 (2015) 374–383, https://doi.org/10.1016/j.surfcoat.2015.06.042.

[70] S.-T. Xiao, S.-M. Wu, Y. Dong, J.-W. Liu, L.-Y. Wang, L. Wu, Y.-X. Zhang, G. Tian, C. Janiak, M. Shalom, Y.-T. Wang, Y.-Z. Li, R.-K. Jia, D.W. Bahnemann, X.-Y. Yang, Rich surface hydroxyl design for nanostructured TiO_2 and its hole-trapping effect, Chem. Eng. J. 400 (2020) 125909, https://doi.org/10.1016/j.cej.2020.125909.

[71] I.V. Keere, R. Willaert, A. Hubin, J. Vereecken, Interaction of human plasma fibrinogen with commercially pure titanium as studied with atomic force microscopy and X-ray photoelectron spectroscopy, Langmuir 24 (2008) 1844–1852, https://doi.org/10.1021/la7016566.

[72] P. Cacciafesta, A.D.L. Humphris, K.D. Jandt, M.J. Miles, Human plasma fibrinogen adsorption on ultraflat titanium oxide surfaces studied with atomic force microscopy, Langmuir 16 (2000) 8167–8175, https://doi.org/10.1021/la000362k.

[73] R.B.L. Bueno, L.N. Teixeira, F.J. Pavinatto, W.M.A. Maximiano, L.R. Zuardi, A. L. Rosa, O.N. Oliveira Jr, S. Spriano, P.T. de Oliveira, Development of calvarial-derived osteogenic cells on GDF-5 coated nanoporous titanium surfaces, Metals 15 (2025) 167, https://doi.org/10.3390/met15020167.

[74] Y. Li, Y. Song, A. Ma, C. Li, Surface immobilization of TiO_2 nanotubes with bone morphogenetic protein-2 synergistically enhances initial preosteoblast adhesion and osseointegration, Biomed. Res. Int. 2019 (2019) 5697250, https://doi.org/10.1155/2019/5697250.

[75] B.S. Kim, H.M. Sung, H.K. You, J. Lee, Effects of fibrinogen concentration on fibrin glue and bone powder scaffolds in bone regeneration, J. Biosci. Bioeng. 118 (2014) 469–475, https://doi.org/10.1016/j.jbiosc.2014.03.014.

[76] R. Kornu, W.J. Maloney, M.A. Kelly, R.L. Smith, Osteoblast adhesion to orthopaedic implant alloys: effects of cell adhesion molecules and diamond-like carbon coating, J. Orthop. Res. 14 (1996) 871–877, https://doi.org/10.1002/jor.1100140605.
[77] A. Noori, S.J. Ashrafi, R. Vaez-Ghaemi, A. Hatamian-Zaremi, T.J. Webster, A review of fibrin and fibrin composites for bone tissue engineering, Int. J. Nanomedicine 12 (2017) 4937–4961, https://doi.org/10.2147/IJN.S124671.
[78] B. Bujoli, J.C. Scimeca, E. Verron, Fibrin as a multipurpose physiological platform for bone tissue engineering and targeted delivery of bioactive compounds, Pharmaceutics. 11 (2019) 556, https://doi.org/10.3390/pharmaceutics11110556.
[79] N. Horasawa, T. Yamashita, S. Uehara, N. Udagawa, High-performance scaffolds on titanium surfaces: osteoblast differentiation and mineralization promoted by a globular fibrinogen layer through cell-autonomous BMP signaling, Mater. Sci. Eng. C Mater. Biol. Appl. 46 (2015) 86–96, https://doi.org/10.1016/j.msec.2014.10.025.
[80] K. Tiedemann, S. Tsao, S.V. Komarova, Platelets and osteoblasts: secretome connections, Am. J. Physiol. Cell Physiol. 323 (2022) C347–C353, https://doi.org/10.1152/ajpcell.00187.2022.
[81] L. Lv, Y. Xie, K. Li, T. Hu, X. Lu, Y. Cao, X. Zheng, Unveiling the mechanism of surface hydrophilicity-modulated macrophage polarization, Adv. Healthc. Mater. 7 (2018) 1800675, https://doi.org/10.1002/adhm.201800675.
[82] R.J. Miron, D.D. Bosshardt, Multinucleated giant cells: good guys or bad guys? Tissue Eng. Part B Rev. 24 (2018) 53–65, https://doi.org/10.1089/ten.TEB.2017.0242.